Research Square

Preprints are preliminary reports that have not undergone peer review.
They should not be considered conclusive, used to inform clinical practice,
or referenced by the media as validated information.

The Deep Earth Origin of the Great Unconformity

Nicolas Flament

nflament@uow.edu.au

University of Wollongong https://orcid.org/0000-0002-3237-0757

Santosh Dhungana

University of Wollongong

Physical Sciences - Article

Keywords:

Posted Date: January 13th, 2026

DOI: https://doi.org/10.21203/rs.3.rs-8246233/v1

License: This work is licensed under a Creative Commons Attribution 4.0 International License.
Read Full License

Additional Declarations: There is **NO** Competing Interest.

Version of Record: A version of this preprint was published at Nature on November 4th, 2026. See the published version at https://doi.org/10.1038/s41586-026-11156-5.

The Deep Earth Origin of the Great Unconformity

Santosh Dhungana[1], Nicolas Flament[1*]

[1]Environmental Futures, School of Science, University of Wollongong, Northfields Avenue, NSW 2522, Australia

Abstract

The Great Unconformity marks a globally extensive erosive surface linked to climatic shifts[1] and environmental transitions[2] that preceded the Cambrian Explosion of life. The processes proposed to explain the formation of the Great Unconformity include glacial erosion during the Snowball Earth[1,3,4], rifting and plume activity[5-7], sea-level fall[8], and mantle-driven dynamic topography[6,9-11]. The dynamics of these processes have not been tested. Here we show that continental-scale uplift and subsidence associated with long-wavelength dynamic topography[12] due to mantle convection drove the formation and preservation of the Great Unconformity. Our models predict prolonged continental-scale Precambrian uplift and long-term Phanerozoic subsidence for Laurentia, Baltica and North China. This vertical motion scenario is ideal for the formation and preservation of the Great Unconformity, which is a first-order surface expression of deep Earth processes. The large area of Laurentia and limited deformation at its margins explain why the Great Unconformity is best preserved and documented there. We show that a single cycle of Precambrian dynamic uplift followed by Phanerozoic dynamic subsidence is the ideal geodynamic scenario for the formation and preservation of the Great Unconformity at continental scale. Our models predict cycles of dynamic topography that are broadly reflected in the preserved sediment volume across continents[1,13].

Main Text

An unconformity is a surface that represents temporal gaps (hiatuses) in the geologic record where younger sediments are deposited over older rocks, after a period of erosion or non-deposition[14]. While unconformities are common in the rock record, they significantly vary in spatial extent and hiatus duration. The largest known unconformity is called the Great Unconformity[15]. It represents a non-depositional hiatus lasting between ~200 million years (Myr) and ~1200 Myr, and marks the onset of sedimentation at the start of Phanerozoic times and of the Cambrian explosion of life[2]. The Great Unconformity was first described in the Grand Canyon[16], and established across North America from a digital database of sedimentary deposits[1,2,9] and thermochronological data[3,4,6,7,10,17]. The base of the Great Unconformity in North America is between 635 Myr old and 482 Myr old (Ediacaran to Early Ordovician times; Fig. 1). Spatially extensive unconformities of a similar age have been documented in Baltica[18-23] and in North China[8,24-27]. Indeed, the global sedimentary volume estimated from geologic maps and borehole data more than doubled across the Precambrian-Phanerozoic boundary[1,13].

The cause or causes of the Great Unconformity are unknown. The proposed mechanisms include extensive glacial erosion during the Snowball Earth (~720–635 Myr ago or Ma)[1,3,4], rifting and plume activity[5-7], sea-level fall[8], and mantle-driven dynamic topography[6,9-11]. These processes have not been dynamically tested, with limited comparison between global models and global datasets. Here we hypothesize that continental-scale dynamic topography[6,9-12,28,29], which is transient over thousands of kilometres and tens of millions of years[12], could generate the continental-scale denudation and sedimentary hiatuses consistent with the geologic record of the Great Unconformity[6,9-11]. Indeed, dynamic uplift followed by dynamic subsidence can produce large-scale erosional surfaces and unconformities[11,12,30]. We test this hypothesis by analysing the evolution of continental dynamic topography predicted by a series of mantle convection models, and comparing it to the volume of sediment preserved on continents over time[1,13].

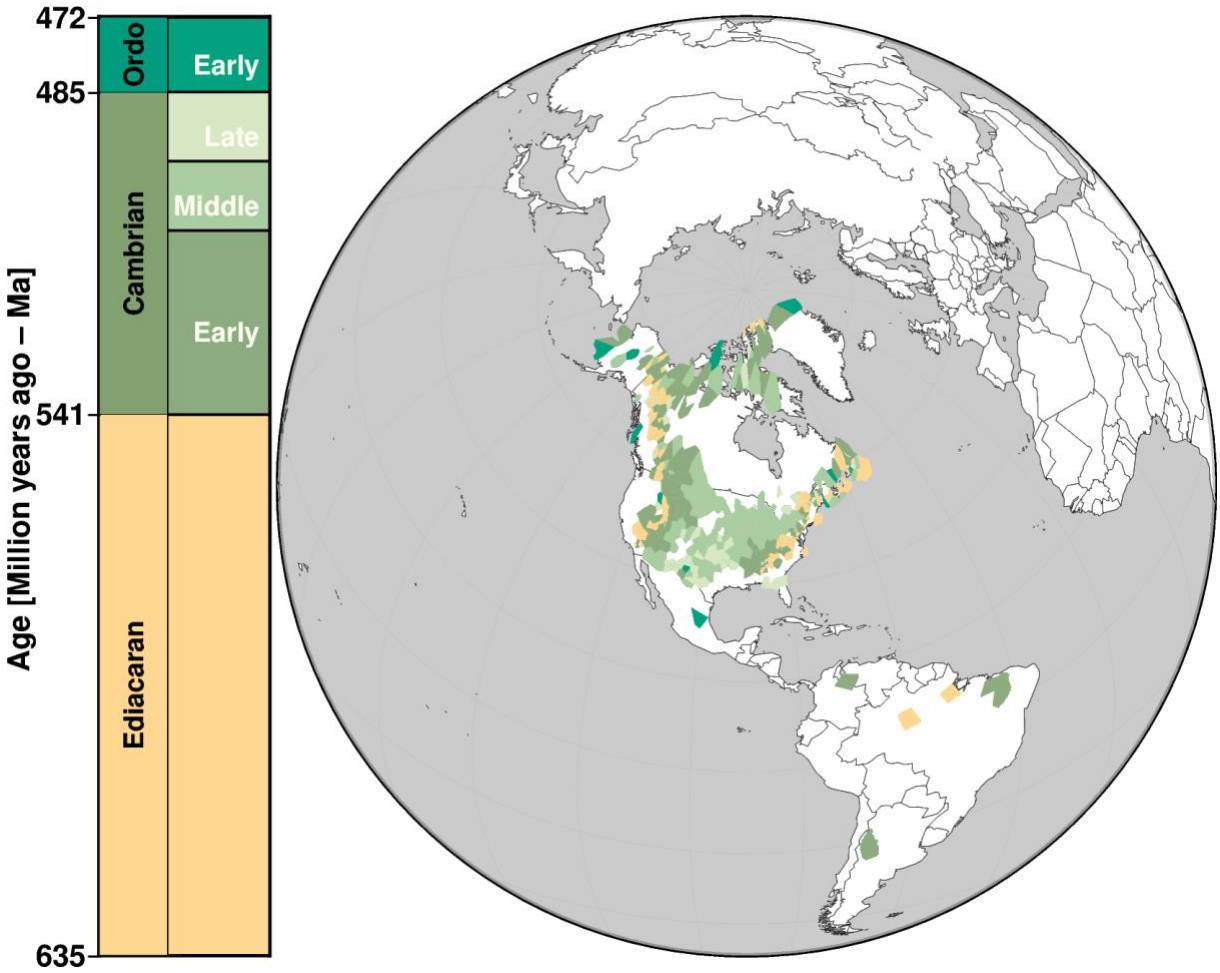


Figure 1 | Oldest sedimentary deposits of the Great Unconformity. Spatial distribution and age of sedimentary strata in the database Macrostrat[31] deposited between Late Ediacaran and Early Ordovician times and coloured by age. Lambert azimuthal equal-area projection at Earth's surface.

Past mantle convection and dynamic topography

To investigate the deep Earth origin of the Great Unconformity, we considered paleogeographically-constrained mantle convection models from one billion years (Gyr ago or Ga). Input parameters were varied across a series of six models (Extended Data Table 1). The models were driven by tectonic reconstructions in the no-net-rotation (NNR) frame of reference (models M2-M6) that is appropriate for mantle convection modelling[32] (Extended Data Figure 1), except for M1 that was based on a paleomagnetic (PMAG) frame of reference. As in previous studies[32,33], we first verified that the Big LOwer-mantle Basal Structures (BLOBS)

predicted by the models were consistent with Large Low-Shear Velocity Provinces (LLSVPs) inferred from ten tomographic models, and that reconstructed volcanic provinces were above or close to the mobile BLOBS predicted by models between 320–0 Ma (Methods; Extended Data Figure 1). Model M6 was preferred because it predicted BLOBS areas and locations consistent with LLSVPs, and volcanic provinces close to BLOBS edges (Extended Data Figure 1).

We investigated the dynamic topography predicted by these mantle flow models between 920–0 Ma. Dynamic topography depends on the distribution of sources of buoyancy and on viscosity. Sources of buoyancy closer to the surface have a greater influence on the amplitude of dynamic topography, and contributions from the deep mantle are most significant at the longest wavelengths[34,35]. We computed dynamic topography from sources of buoyancy and viscosity variations deeper than 350 km depth[29]. This setup resulted in smooth dynamic topography (Fig. 2a-b) at the continental scale[29,36], which was desirable to test the hypothesis that the Great Unconformity could be linked to mantle flow. However, the setup is known to overpredict the amplitude of long-wavelength dynamic topography by a factor of about two[29,36]. We therefore focused on the trend of dynamic topography evolution, which was key to our analysis, as opposed to the amplitude of dynamic topography.

The motion of tectonic plates and subduction zones affected mantle convection and dynamic topography[12,28,32,33,36,37] (Fig. 2, Supplementary Video 1). At 640 Ma, dynamic topography exhibited a north-south hemispheric planform with positive dynamic topography beneath Laurentia, Baltica, North China, Amazonia, Australia, Kalahari, and Antarctica (Fig. 2a), which were above a BLOBS in the southern hemisphere (Fig. 2c). Laurentia was tilted down to the southwest, positioned above a BLOBS and whole-mantle upwelling (Fig. 2e). The motion of tectonic blocks between 640–440 Ma reorganized mantle convection (Supplementary Video 1) so that by 440 Ma, the hemispheric planform of dynamic topography was oriented east-west, with negative dynamic topography beneath most continental blocks to the notable exceptions of Laurentia and Baltica (Fig. 2b). Laurentia was tilted down to the

southeast, above subduction-driven downwelling along its eastern margin and above a BLOBS and whole-mantle upwelling in the west (Fig. 2f).

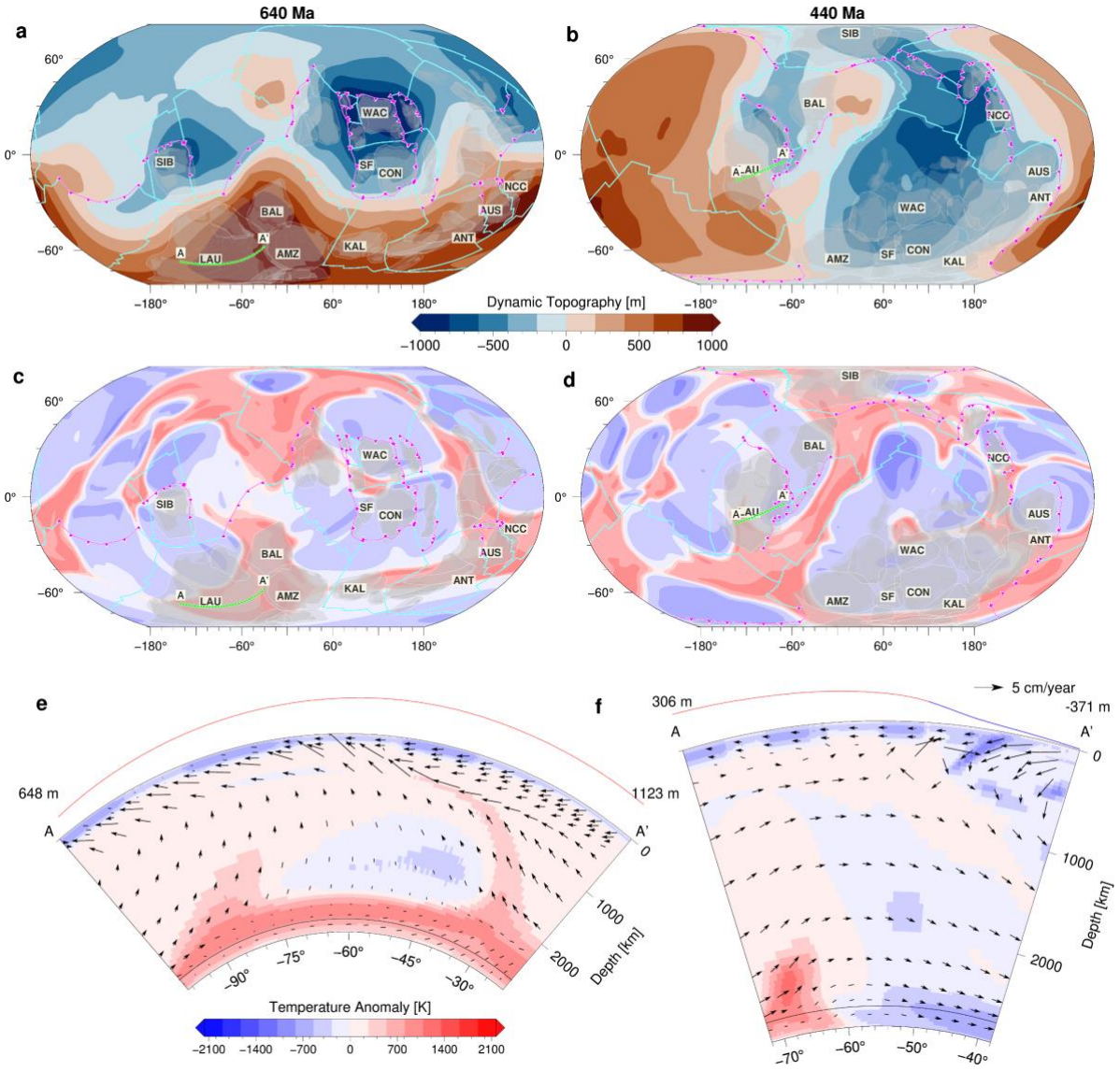


Figure 2 | Predicted joint evolution of dynamic topography and mantle temperature. a-b, Dynamic topography at 640 Ma (**a**) and 440 Ma (**b**). **c-d**, Mantle temperature anomaly at 2,677 km depth at 640 Ma (**c**) and 440 Ma (**d**). In **a-d**, cyan lines represent mid-ocean ridges and transform faults and magenta lines represent subduction zones with triangles on the overriding plate. Transparent grey polygons represent continental blocks, with labels 'AMZ': Amazonia, 'ANT': Antarctica, 'AUS': Australia, 'BAL': Baltica, 'CON': Congo, KAL: Kalahari, 'LAU': Laurentia, 'NCC': North China, 'SF': São Francisco, 'SIB': Siberia and 'WAC': West Africa. The green lines with diamonds are great circles transects A-A' shown in **e-f**. The length of the great circle depends on its latitudinal position. Robinson projection at Earth's surface. **e-f**, Cross-sections of temperature anomalies and dynamic topography across Laurentia (transect A-A'). The colour bar in (**e**) is the temperature anomaly scale for **c-f**. Black arrows are velocity vectors. The amplitude of dynamic topography (not to scale) is represented

above the cross-sections with positive amplitudes in red, negative amplitudes in blue, and reported values at A and A'. The black solid line indicates 2,667 km depth. Polar projection of longitude and depth.

Formation and preservation of the Great Unconformity

We used *k*-means cluster analysis to quantify the spatial and temporal evolution of continental dynamic topography during the formation (920–420 Ma) and preservation (420–0 Ma) of the Great Unconformity (Methods; Fig. 3). We established that considering two clusters for each period was most representative for most considered model cases except M4 for which three clusters were appropriate (Methods and Extended Data Figure 2). These clusters, which we represented in the present-day continental configuration, captured regions in which dynamic topography evolved similarly over time (Fig. 3 and Extended Data Figure 3).

For the period 920–420 Ma, the main continental blocks in cluster GU-F ('Great Unconformity - Formation') were Laurentia, Baltica, northeastern North China, most of South America, western Australia, the Kalahari craton and parts of Antarctica. Cluster GU-NF ('Great Unconformity - No Formation') spanned most of Africa, Asia, parts of Antarctica, and the São Francisco Craton (Fig. 3a). Cluster GU-F captured positive dynamic topography (Fig. 3d), mainly above whole-mantle upwelling (Supplementary Video 1). Dynamic topography was relatively stable between 900–800 Ma, increased rapidly between 800–720 Ma, followed by a gradual increase between 720–600 Ma, and a rapid decrease between 600–420 Ma (Fig. 3d). The predicted uplift would have promoted glacial erosion[1] during the proposed Sturtian and Marinoan global glaciations (Fig. 3d). The GU-F pattern of prolonged dynamic uplift during Precambrian times (Fig. 2 and Supplementary Video 2), followed by dynamic subsidence during Cambrian times (Fig. 3d) was consistent across all mantle convection models (Extended Data Figures 3 and 4a). Cluster GU-NF captured dynamic topography on average negative throughout 920–420 Ma with gradual increase between 900–760 Ma, a rapid decline between 760–520 Ma, and renewed increase between 520–420 Ma (Fig. 3d). In cluster GU-NF, Siberia, and the Congo and West African cratons were in a

dynamic topography low surrounded by subduction zones (Fig. 2a, c and Supplementary Video 1).

For the period 420–0 Ma, cluster GU-HPP ('Great Unconformity-High Preservation Potential') spanned Western Laurentia, Baltica, North China, and Siberia and cluster GU-LPP ('Great Unconformity-Low Preservation Potential') spanned Eastern Laurentia, Africa, Australia, Antarctica, and India (Fig. 3b). The dynamic topography for GU-HPP, which was generally negative due to subduction (Supplementary Video 1), remained relatively stable between 420–240 Ma, before gradually declining until 0 Ma (Fig. 3e). In contrast, in GU-LPP dynamic topography increased between 420–240 Ma, was stable between 240–120 Ma, then gradually declined until 0 Ma (Fig. 3e).

We derived a map highlighting the areas in which the Great Unconformity was predicted to have formed and to have a high preservation potential, which consisted of Laurentia, Baltica and northeastern North China for model M6 (Fig. 3c) and across varying areas around Laurentia and Baltica in all six models (Extended Data Figures 4-5). We analysed the sensitivity of these results to the number of clusters (either two or three) for each period (formation 920–420 Ma, preservation from 420 Ma) from vote maps (Methods) of areas in which the Great Unconformity was predicted to exist across the six models (Extended Data Figure 6). This confirmed that Laurentia, Baltica and North China were the main continental blocks in which the Great Unconformity was predicted to have formed and to be preserved, with northern South America and northern Australia emerging as two possible additional regions (Extended Data Figure 6).

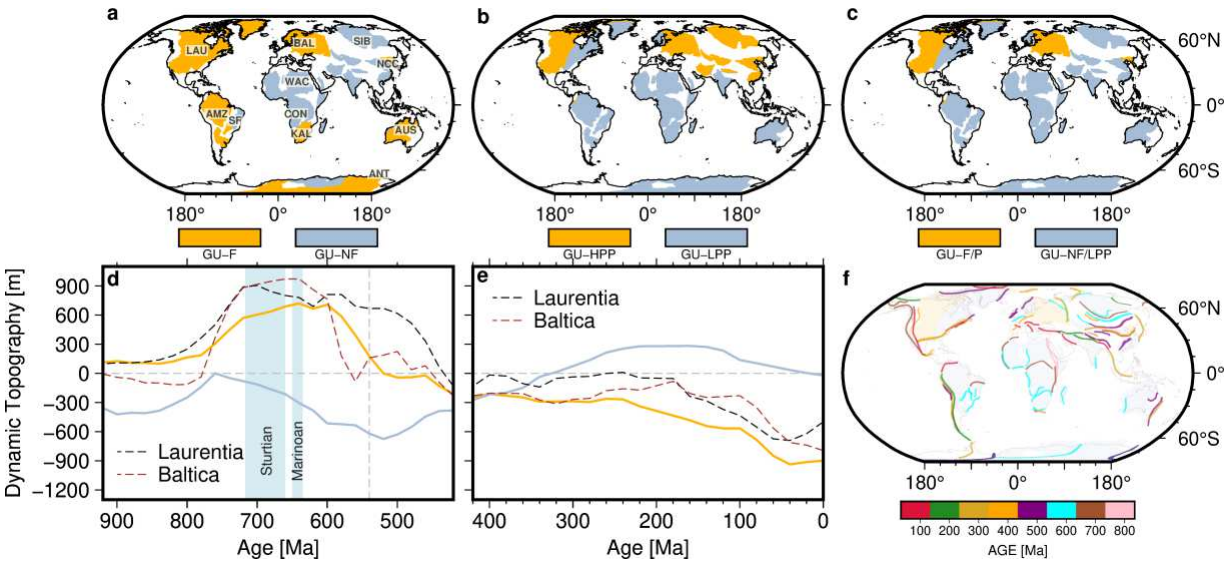


Figure 3 | Spatio-temporal evolution of dynamic topography. a-c, Spatial distribution of two clusters across continental blocks that existed from 920 Ma. **a**, GU-F ('Great Unconformity - Formation') and GU-NF ('Great Unconformity - Non Formation') between 920–420 Ma; **b**, GU-HPP ('Great Unconformity - High Preservation Potential') and GU-LPP ('Great Unconformity - Low Preservation Potential') from 420 Ma; and **c**, regions in which the Great Unconformity was formed and preserved ('GU-F/P') as opposed to regions with low formation and preservation potential ('GU-NF/LPP'). Robinson projection at Earth's surface. **d-e**, Temporal evolution of averaged continental dynamic topography for each cluster in **a** and **b**, respectively. The black and brown dashed line represent the average dynamic topography for Laurentia and Baltica, respectively. The light blue shaded polygons represent the duration of the two main glaciations during Cryogenian ages, the vertical dashed line represents the start of Cambrian times, and the horizontal dashed line represents the datum for dynamic topography. **f**, Locations of orogens[38] from 900 Ma (coloured by age in 100 Ma interval). Robinson projection at Earth's surface.

Linking dynamic topography to preserved sediment flux for each continent

We verified that the dynamic topography evolution predicted by our models was consistent with the preserved sediment flux for each continent except Africa[1,13] (Methods; Fig. 4). Predicted prolonged Precambrian uplift followed by rapid Cambrian subsidence generally matched increased sediment flux across the Precambrian-Cambrian boundary (Fig. 4a). A shift from erosion to sedimentation reflecting decreasing dynamic topography (Fig. 4) and flooded continents (Extended Data Figure 7a) was predicted for all continents except for Eurasia and Africa that consisted of tectonic blocks with contrasted Neoproterozoic

183 histories. In Eurasia, dynamic uplift was predicted for Baltica and North China, and dynamic
184 subsidence for Siberia[39] (Fig. 4a and Extended Data Figures 8 and 9). In Africa, dynamic uplift
185 was predicted for the Kalahari Craton, and dynamic subsidence for the Congo and West
186 African cratons (Extended Data Figures 8 and 9) was consistent with their sedimentary record
187 of long-lived depocenters[40,41]. Extensive Precambrian orogens within Africa enhanced erosion
188 and sedimentation (Fig. 3f and Extended Data Figure 7), leading to a landscape in which
189 negative dynamic topography did not result in increased sediment flux at the base of Cambrian
190 times (Extended Data Figure 7a).

191 The evolution of predicted Phanerozoic dynamic topography differed across
192 continental blocks. Laurentia, Baltica and North China were characterized by sustained
193 dynamic subsidence, which aligned with increased preserved sediment flux across North
194 America and Eurasia (Fig. 4). Conversely, predicted renewed dynamic uplift of South America
195 and of Australia, which would have eroded earlier unconformities[11,30] and formed new ones,
196 corresponded to decreased preserved sediment flux (Fig. 4).

197 Importantly, the number of dynamic topography uplift-subsidence cycles governed the
198 formation and preservation of the Great Unconformity. A single cycle of Precambrian uplift
199 followed by Phanerozoic subsidence was the ideal scenario to form and preserve the Great
200 Unconformity. This scenario was predicted for Laurentia for all models (Fig. 4b and Extended
201 Data Figure 9a), in first-order agreement with thermochronology studies[3,4,7,10,17]. The scenario
202 was also predicted for Baltica and North China for most models (Extended Data Figure 9a-b):
203 Precambrian uplift was not systematically predicted for Baltica and North China, and it varied
204 in amplitude between models (Extended Data Figure 9b). Interestingly, all models predicted
205 dynamic uplift of Baltica as it moved from the south hemisphere to the north hemisphere
206 between 540–520 Ma (Supplementary Video 1), followed by rapid subsidence consistent with
207 sub-Cambrian unconformity linked to epeirogenic uplift[21,42].

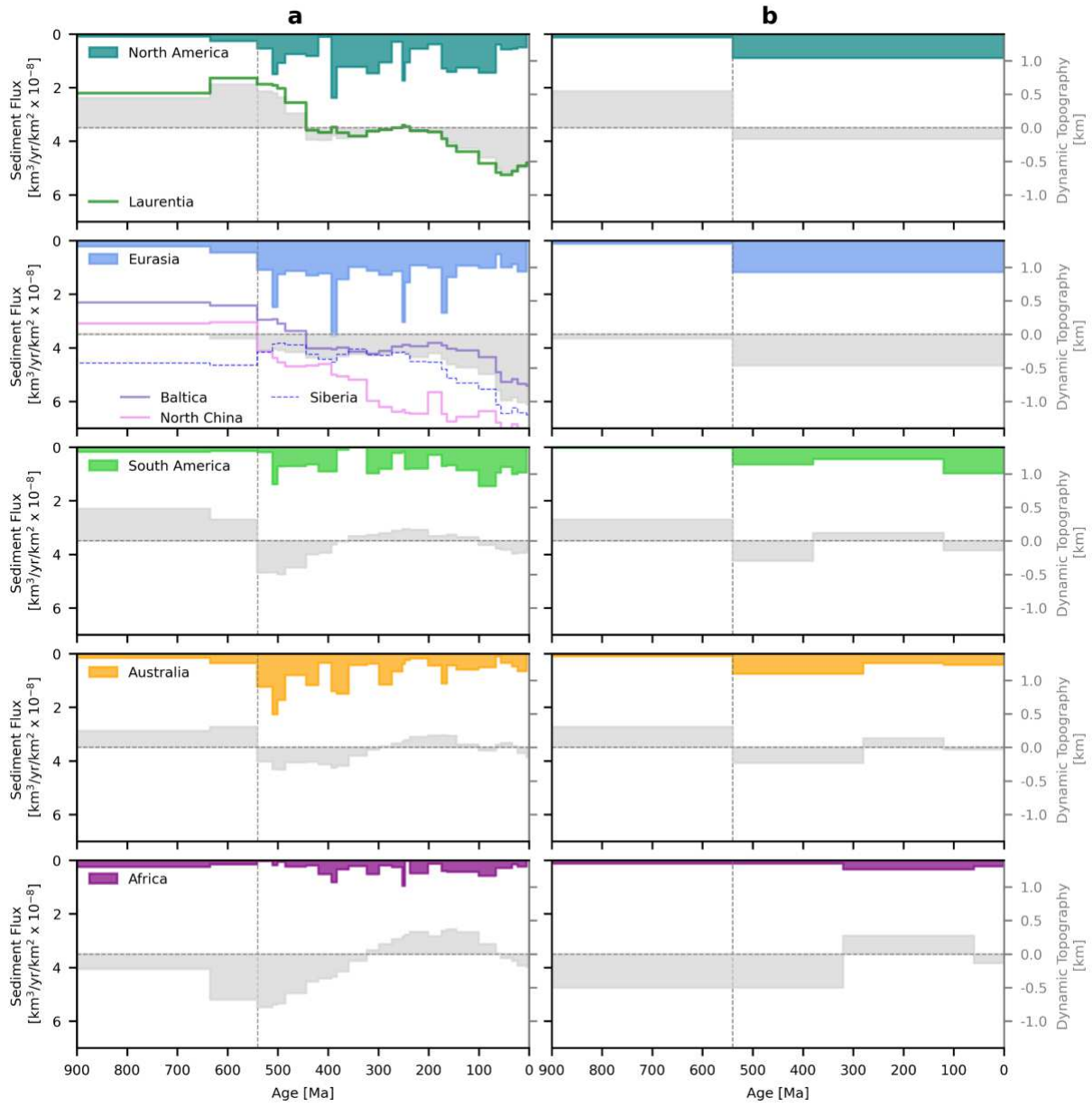


Figure 4 | Volumetric flux of preserved sediments and average dynamic topography for each continent. a, Evolution of the preserved volume of sediment per year and per unit continental area (increasing down), and dynamic topography for each continent averaged at time steps corresponding to the sediment preservation data[1,13]. Coloured solid and dotted lines represent the evolution of dynamic topography for Laurentia and continental blocks in Eurasia. **b**, Data in **a** temporally averaged for dynamic topography cycles in each continent.

In contrast, most models predicted two cycles of dynamic uplift followed by dynamic subsidence for South America and Australia (Fig. 4b and Extended Data Figure 9c-d) and long-lived dynamic subsidence followed by dynamic uplift then renewed dynamic subsidence for

Africa (Fig. 4b and Extended Data Figure 9c-d), consistent with thermochronological and geochronological evidence for these regions[43-47]. The predicted dynamic uplift of South America and Australia coincided with preserved sediment flux on these continents, as expected (Fig. 4b and Extended Data Figure 9c-d). However, the dynamic uplift of Africa coincided with increased sediment preservation, because Africa was positioned centrally in Gondwana (Extended Data Figure 7b) and orogens in Antarctica and South America (Fig. 3f) restricted drainage from Africa to the oceans, leading to endorheic (inland) sedimentation[48].

Geodynamic and tectonic drivers of the Great Unconformity

Comparing dynamic topography cycles to preserved sediment flux confirmed Laurentia, Baltica and North China as continental blocks on which the Great Unconformity was predicted to have formed and to be preserved (Fig. 4). Interestingly, the Great Unconformity surface is exposed and extensively studied in Laurentia[1,3,5-7,9,10,14,17] and in North China[8,24-27], whereas it is mostly inferred to occur beneath younger sediments in Baltica[18-23]. This largely stems from the tectonic and geodynamic evolution of each of these continental blocks. In the considered tectonic scenario, Baltica and Laurentia were independent from other blocks without active subduction along their margins between 540–440 Ma and 540–500 Ma, respectively (Supplementary Video 1). Subduction beneath north and east Laurentia from ~500 Ma and southeast Baltica from ~460 Ma resulted in their amalgamation into Laurussia by ~420 Ma, associated with continent-wide Cambrian transgression (Extended Data Figure 7a, Supplementary Video 1). North China was on the periphery of Gondwana during Cambrian times with a subduction zone at its western margin (Fig. 4a and c and Supplementary Video). During the assembly of Pangea, collision occurred along some of the margins of all three continental blocks (Fig. 3f, Extended Data Figure 7b), promoting the deformation and erosion of rocks potentially preserving the Great Unconformity, or their burial in foreland basins. The large continental area of Laurentia and limited reworking at its margins were favourable to record the formation of the continental-scale Great Unconformity. The prominent exposure of

246 the Great Unconformity in the Grand Canyon[14-16] has been linked to the Laramide uplift event
247 from Farallon flat-slab subduction and subsequent Colorado River incision[49,50]. Repeated
248 orogeny along the eastern margin of Baltica (Fig. 3f) could explain why the Great
249 Unconformity is generally inferred to occur at depth on that smaller continental block. Early
250 Cretaceous lithospheric delamination[51] could explain the exposure of the Great Unconformity
251 in North China, which is unexpected given its comparatively small area and four episodes of
252 orogenesis between ~500 Ma and ~200 Ma (Fig. 3f).

253 The changes in dynamic topography over ~20 Myr and ~5,000 km predicted by our
254 models suggest that the motion of continents over the convecting mantle provided the large-
255 scale geodynamic environments that favoured the formation and preservation of the Great
256 Unconformity in Laurentia, Baltica and North China. The geologic record of uplift[4-7,10] and
257 subsidence[4-7,9,10,19] indicates that the timing of erosion and deposition[52] varied between
258 locations, which likely reflects the effect of processes such as tectonic deformation and flexure
259 that would affect relative sea level over shorter spatial and temporal scales.

260 Our models explain why the Great Unconformity is best preserved in North America
261 and show that the Great Unconformity is a first-order surface expression of deep geodynamic
262 processes that transformed global landscapes and sediment fluxes. In turn, these landscape
263 dynamics would have altered seawater chemistry and catalysed the Cambrian explosion of
264 life[2]. A new opportunity is opening in Earth system modelling to unravel the geodynamic
265 environments of the evolution of complex life by coupling billion-year reconstructions of
266 Earth's evolving deep interior and landscapes to the evolution of global sediment fluxes, sea
267 water chemistry, and diversification of life forms.

268

References

1 Keller, C. B. *et al.* Neoproterozoic glacial origin of the Great Unconformity. *Proceedings of the National Academy of Sciences* **116**, 1136-1145 (2019). https://doi.org/10.1073/pnas.1804350116

2 Peters, S. E. & Gaines, R. R. Formation of the 'Great Unconformity' as a trigger for the Cambrian explosion. *Nature* **484**, 363-366 (2012). https://doi.org/10.1038/nature10969

3 McDannell, K. T. & Keller, C. B. Cryogenian glacial erosion of the central Canadian Shield: The "late" Great Unconformity on thin ice. *Geology* **50**, 1336-1340 (2022). https://doi.org/10.1130/G50315.1

4 McDannell, K. T., Keller, C. B., Guenthner, W. R., Zeitler, P. K. & Shuster, D. L. Thermochronologic constraints on the origin of the Great Unconformity. *Proceedings of the National Academy of Sciences* **119**, e2118682119 (2022). https://doi.org/10.1073/pnas.2118682119

5 Sturrock, C. P., Flowers, R. M. & Macdonald, F. A. The Late Great Unconformity of the Central Canadian Shield. *Geochemistry, Geophysics, Geosystems* **22**, e2020GC009567 (2021). https://doi.org/https://doi.org/10.1029/2020GC009567

6 Peak, B. A., Flowers, R. M. & Macdonald, F. A. Ediacaran-Ordovician tectonic and geodynamic drivers of Great Unconformity exhumation on the southern Canadian Shield. *Earth and Planetary Science Letters* **619**, 118334 (2023). https://doi.org/https://doi.org/10.1016/j.epsl.2023.118334

7 Flowers, R. M., Macdonald, F. A., Siddoway, C. S. & Havranek, R. Diachronous development of Great Unconformities before Neoproterozoic Snowball Earth. *Proceedings of the National Academy of Sciences* **117**, 10172-10180 (2020). https://doi.org/10.1073/pnas.1913131117

8 Sun, Y. *et al.* Global sea-level fall triggered Ediacaran–Cambrian unconformity in North China craton. *Earth and Planetary Science Letters* **622**, 118411 (2023). https://doi.org/https://doi.org/10.1016/j.epsl.2023.118411

9 Tasistro-Hart, A. R. & Macdonald, F. A. Phanerozoic flooding of North America and the Great Unconformity. *Proceedings of the National Academy of Sciences* **120**, e2309084120 (2023). https://doi.org/10.1073/pnas.2309084120

10 DeLucia, M. S., Guenthner, W. R., Marshak, S., Thomson, S. N. & Ault, A. K. Thermochronology links denudation of the Great Unconformity surface to the supercontinent cycle and snowball Earth. *Geology* **46**, 167-170 (2018). https://doi.org/https://doi.org/10.1130/G39525.1

11 Burgess, P. M., Gurnis, M. & Moresi, L. Formation of sequences in the cratonic interior of North America by interaction between mantle, eustatic, and stratigraphic processes. *GSA Bulletin* **109**, 1515-1535 (1997). https://doi.org/10.1130/0016-7606(1997)109<1515:FOSITC>2.3.CO;2

12 Flament, N., Gurnis, M. & Müller, R. D. A review of observations and models of dynamic topography. *Lithosphere* **5**, 189-210 (2013). https://doi.org/10.1130/L245.1

13 Ronov, A. B., Khain, V. E., Balukhovsky, A. N. & Seslavinsky, K. B. Quantitative analysis of Phanerozoic sedimentation. *Sedimentary Geology* **25**, 311-325 (1980). https://doi.org/https://doi.org/10.1016/0037-0738(80)90067-6

14 Karlstrom, K. E. & Timmons, J. M. in *Grand Canyon Geology: Two Billion Years of Earth's History* (eds J. Michael Timmons & Karl E. Karlstrom) 0 (Geological Society of America, 2012).

15 Dutton, C. E. Tertiary history of the Grand Canon District, with atlas. *Monograph* (1882). https://doi.org/10.3133/m2

16 Powell, J. W., Thompson, A. H., Coues, E. & Goode, G. B. *Exploration of the Colorado River of the West and Its Tributaries: Explored in 1869, 1870, 1871, and 1872, Under*

the Direction of the Secretary of the Smithsonian Institution. (US government printing office, 1875).

17 Peak, B. A., Flowers, R. M., Macdonald, F. A. & Cottle, J. M. Zircon (U-Th)/He thermochronology reveals pre-Great Unconformity paleotopography in the Grand Canyon region, USA. *Geology* **49**, 1462-1466 (2021). https://doi.org/10.1130/G49116.1

18 Valverde-Vaquero, P. *et al.* U–Pb single-grain dating of detrital zircon in the Cambrian of central Poland: implications for Gondwana versus Baltica provenance studies. *Earth and Planetary Science Letters* **184**, 225-240 (2000). https://doi.org/https://doi.org/10.1016/S0012-821X(00)00312-5

19 Kukkonen, I. T. *et al.* Phanerozoic evolution of Fennoscandia: Evidence from apatite fission track, fluid flow and geodynamic data in Finland and Estonia. *Gondwana Research* **146**, 74-92 (2025). https://doi.org/https://doi.org/10.1016/j.gr.2025.05.011

20 Grendaitė, M., Michelevičius, D. & Radzevičius, S. Insights into the structural geology and sedimentary succession of the Baltic Basin, Western Lithuania. *Marine and Petroleum Geology* **147**, 106009 (2023). https://doi.org/https://doi.org/10.1016/j.marpetgeo.2022.106009

21 Hall, A. M. *et al. The sub-Cambrian unconformity in Västergötland, Sweden: reference surface for Pleistocene glacial erosion of basement*. (Svensk Kärnbränslehantering AB, 2019).

22 Nielsen, A. & Schovsbo, N. Cambrian to basal Ordovician lithostratigraphy in Southern Scandinavia. *Bulletin of the Geological Society of Denmark* **53**, 47-92 (2006). https://doi.org/10.37570/bgsd-2006-53-04

23 Murrell, G. R. & Andriessen, P. A. M. Unravelling a long-term multi-event thermal record in the cratonic interior of southern Finland through apatite fission track thermochronology. *Physics and Chemistry of the Earth, Parts A/B/C* **29**, 695-706 (2004). https://doi.org/https://doi.org/10.1016/j.pce.2004.03.007

24 Sun, Y. *et al.* Detrital zircon geochronology and stratigraphy of the Proterozoic strata in the Olongbuluke terrane of Northwest China: Implications for the Great Unconformity. *Precambrian Research* **376**, 106684 (2022). https://doi.org/https://doi.org/10.1016/j.precamres.2022.106684

25 Lee, J.-H. *et al.* The Great Unconformity in the eastern Sino-Korean Block: A synthesis of Taebaek Group stratigraphy, fault controls, and global correlations. *Earth-Science Reviews* **270**, 105244 (2025). https://doi.org/https://doi.org/10.1016/j.earscirev.2025.105244

26 Li, M. *et al.* A window into the Great Unconformity: Insights from geochemistry and geochronology of Ediacaran glaciogenic rocks in the North China Craton. *Journal of Asian Earth Sciences* **194**, 104327 (2020). https://doi.org/https://doi.org/10.1016/j.jseaes.2020.104327

27 Wan, B. *et al.* Repositioning the Great Unconformity at the southeastern margin of the North China Craton. *Precambrian Research* **324**, 1-17 (2019). https://doi.org/https://doi.org/10.1016/j.precamres.2019.01.014

28 Spasojevic, S. & Gurnis, M. Sea level and vertical motion of continents from dynamic earth models since the Late Cretaceous. *AAPG Bulletin* **96**, 2037-2064 (2012). https://doi.org/10.1306/03261211121

29 Flament, N. Present-day dynamic topography and lower-mantle structure from palaeogeographically constrained mantle flow models. *Geophysical Journal International* **216**, 2158-2182 (2019). https://doi.org/10.1093/gji/ggy526

30 Braun, J., Robert, X. & Simon-Labric, T. Eroding dynamic topography. *Geophysical Research Letters* **40**, 1494-1499 (2013). https://doi.org/https://doi.org/10.1002/grl.50310

31 Peters, S. E., Husson, J. M. & Czaplewski, J. Macrostrat: A Platform for Geological Data Integration and Deep-Time Earth Crust Research. *Geochemistry, Geophysics,*

Geosystems **19**, 1393-1409 (2018). https://doi.org/https://doi.org/10.1029/2018GC007467

32 Flament, N., Bodur, Ö. F., Williams, S. E. & Merdith, A. S. Assembly of the basal mantle structure beneath Africa. *Nature* **603**, 846-851 (2022). https://doi.org/10.1038/s41586-022-04538-y

33 Cucchiaro, A., Flament, N., Arnould, M. & Cressie, N. Large volcanic eruptions are mostly sourced above mobile basal mantle structures. *Communications Earth & Environment* **6**, 538 (2025). https://doi.org/10.1038/s43247-025-02482-z

34 Hager, B. H. & Clayton, R. W. Constraints on the structure of mantle convection using seismic observations, flow models, and the geoid. *Mantle convection* **657** (1989).

35 Colli, L., Ghelichkhan, S. & Bunge, H.-P. On the ratio of dynamic topography and gravity anomalies in a dynamic Earth. *Geophysical Research Letters* **43**, 2510-2516 (2016). https://doi.org/https://doi.org/10.1002/2016GL067929

36 Davies, D. R. *et al.* Earth's multi-scale topographic response to global mantle flow. *Nature Geoscience* **12**, 845-850 (2019). https://doi.org/10.1038/s41561-019-0441-4

37 Cao, X., Flament, N., Bodur, Ö. F. & Müller, R. D. The evolution of basal mantle structure in response to supercontinent aggregation and dispersal. *Scientific Reports* **11**, 22967 (2021). https://doi.org/10.1038/s41598-021-02359-z

38 Condie, K. C., Pisarevsky, S. A. & Puetz, S. J. LIPs, orogens and supercontinents: The ongoing saga. *Gondwana Research* **96**, 105-121 (2021). https://doi.org/https://doi.org/10.1016/j.gr.2021.05.002

39 Frolov, S. V. *et al.* Meso-Neoproterozoic petroleum systems of the Eastern Siberian sedimentary basins. *Precambrian Research* **259**, 95-113 (2015). https://doi.org/https://doi.org/10.1016/j.precamres.2014.11.018

40 Delvaux, D., Maddaloni, F., Tesauro, M. & Braitenberg, C. The Congo Basin: Stratigraphy and subsurface structure defined by regional seismic reflection, refraction and well data. *Global and Planetary Change* **198**, 103407 (2021). https://doi.org/https://doi.org/10.1016/j.gloplacha.2020.103407

41 Kalsbeek, F. & Frei, R. Geochemistry of Precambrian sedimentary rocks used to solve stratigraphical problems: An example from the Neoproterozoic Volta basin, Ghana. *Precambrian Research* **176**, 65-76 (2010). https://doi.org/https://doi.org/10.1016/j.precamres.2009.10.004

42 Nielsen, A. T. & Schovsbo, N. H. The regressive Early-Mid Cambrian 'Hawke Bay Event' in Baltoscandia: Epeirogenic uplift in concert with eustasy. *Earth-Science Reviews* **151**, 288-350 (2015). https://doi.org/https://doi.org/10.1016/j.earscirev.2015.09.012

43 Morón, S. *et al.* Denuding a Craton: Thermochronology Record of Phanerozoic Unroofing From the Pilbara Craton, Australia. *Tectonics* **39**, e2019TC005988 (2020). https://doi.org/https://doi.org/10.1029/2019TC005988

44 Kohn, B. P. *et al.* Shaping the Australian crust over the last 300 million years: Insights from fission track thermotectonic imaging and denudation studies of key terranes. *Australian Journal of Earth Sciences* **49**, 697-717 (2002). https://doi.org/10.1046/j.1440-0952.2002.00942.x

45 Flowers, R. M. & Schoene, B. (U-Th)/He thermochronometry constraints on unroofing of the eastern Kaapvaal craton and significance for uplift of the southern African Plateau. *Geology* **38**, 827-830 (2010). https://doi.org/10.1130/g30980.1

46 Fonseca, A., Nachtergaele, S., Bonilla, A., Dewaele, S. & De Grave, J. Extensional exhumation of cratons: insights from the Early Cretaceous Rio Negro–Juruena belt (Amazonian Craton, Colombia). *Solid Earth* **15**, 329-352 (2024). https://doi.org/10.5194/se-15-329-2024

47 Japsen, P., Green, P. F. & Bonow, J. M. Ups and downs of the Guiana Shield and Amazon Basin over the last 500 Myr. *Gondwana Research* **148**, 415-444 (2025). https://doi.org/https://doi.org/10.1016/j.gr.2025.06.020

48 Salles, T., Husson, L., Lorcery, M. & Hadler Boggiani, B. Landscape dynamics and the Phanerozoic diversification of the biosphere. *Nature* **624**, 115-121 (2023). https://doi.org/10.1038/s41586-023-06777-z

49 Karlstrom, K. E. *et al.* Formation of the Grand Canyon 5 to 6 million years ago through integration of older palaeocanyons. *Nature Geoscience* **7**, 239-244 (2014). https://doi.org/10.1038/ngeo2065

50 Liu, L. *et al.* The role of oceanic plateau subduction in the Laramide orogeny. *Nature Geoscience* **3**, 353-357 (2010). https://doi.org/10.1038/ngeo829

51 Wu, F.-Y., Yang, J.-H., Xu, Y.-G., Wilde, S. A. & Walker, R. J. Destruction of the North China Craton in the Mesozoic. *Annual Review of Earth and Planetary Sciences* **47**, 173-195 (2019). https://doi.org/https://doi.org/10.1146/annurev-earth-053018-060342

52 Shahkarami, S., Buatois, L. A., Mángano, M. G., Hagadorn, J. W. & Almond, J. The Ediacaran–Cambrian boundary: Evaluating stratigraphic completeness and the Great Unconformity. *Precambrian Research* **345**, 105721 (2020). https://doi.org/https://doi.org/10.1016/j.precamres.2020.105721

Methods

Macrostrat

Macrostrat is an open, relational geospatial database that enables large-scale, quantitative analysis of 33,903 lithologically and chronologically defined rock units across 1,474 regions in the Americas, New Zealand, and the deep sea[31].

We accessed lithostratigraphic data from the Macrostrat (https://macrostrat.org/api/units/?lith_class=sedimentary) database via API (v2). We downloaded sedimentary units and associated stratigraphic columns as geoJSON files in June 2025. We created map of transgressive sequences and erosional remnants across North America and northern South America (Fig. 1) spanning late Neoproterozoic to early Ordovician times.

Mantle convection models

We used the code *CitcomS*[53] to model mantle convection for a billion years (1,000–0 Ma). In *CitcomS,* the mantle structure is represented with finite-element nodes in 3D spherical geometry. We considered six model cases (Extended Data Table 1), five of which have been presented in previous work (M1 was C12 in ref. 32; M2 was C1 in ref. 54; M3 was C5 in ref. 32; M4 was C3 in ref. 54, C20 in ref. 32 and C3 in ref. 55; and M5 was MF in ref. 56).

We discretised the mantle into ~13 million nodes (129 × 129 × 65 × 12), with radial mesh refinements at the surface (~ 50 × 50 × 15 km) and core-mantle boundary (CMB; ~28 × 28 × 27 km) and relatively lower resolution in the mid-mantle (~40 × 40 × 100 km). We reconstructed mantle flow in a modified version of *CitcomS*[53,57] that progressively assimilated plate kinematics, obtained from tectonic reconstructions[58] with continuously closing plate polygons[59], as time-dependent boundary conditions in one million year increments. We used the extended-Boussinesq approximation that assumed the mantle to be an incompressible fluid to account for viscous dissipation, internal heating, depth-dependent thermal expansion coefficient and an adiabatic temperature gradient[60].

For initial boundary conditions and time-progressive data assimilation, we created a lithospheric thermal structure from reconstructed seafloor ages and the half-space cooling with a maximum seafloor age set equal to 80 Myr to obtain a maximum thickness of oceanic lithosphere consistent with observations for the present day. We used the method of ref. 61 to reconstruct synthetic seafloor ages while the continental lithosphere adopted simplified tectonothermal ages from ref. 62. The global thermal regime of continental lithosphere and subducting slabs, reconstructed using seafloor ages and location of subduction zones[63], were incorporated into the flow models in one million year increments.

The initial conditions included an adiabatic temperature profile between two boundary layers: the lithosphere at the surface, and a 225 km thick laterally uniform basal layer containing a 113 km thick layer with excess density. The density contrast $\delta\rho_b$ between the basal layer and the ambient mantle was defined by the buoyancy ratio $B = \frac{\delta\rho_b}{\rho\alpha\Delta T}$ where ΔT = 4,300 K was the temperature change across mantle, ρ = 5,546 kg m^{-3} was the average density[64] and $\alpha = 1.32 \times 10^{-5}$ K^{-1} was thermal expansivity[65] in the 100 km layer above the CMB. The initial condition consisted of slabs inserted down to 550 km depth for models M1-M2 (1,000 km for models M3,5-6 and 1,200 km for M4) with dip angles of 45° dip down to 425 km depth and 90° descent below. To incorporate the advective thickening of more viscous lower mantle, lower mantle slabs were twice as thick as upper mantle slabs in the initial condition. Models were initialized with differing warm-up phases lasting 200 Myr for model M2, 250 Myr for models M5-6 and 0 Myr for other models (Extended Data Table 1) using the 1 Ga configuration for tectonic velocities, subduction zones positions and lithospheric age. Boundary conditions were isothermal (T = 273K at the surface and T = 3,373K at the CMB), imposed plate kinematics (velocities) at the surface, and free-slip kinematic condition at the CMB.

The convective vigour in models was governed by the Rayleigh number $Ra = \frac{\alpha_0\rho_0 g_0 \Delta T h_M^3}{\kappa_0\eta_0}$, where $\alpha_0 = 3 \times 10^{-5}$ K^{-1} was the coefficient of thermal expansion at the surface,

$\rho_0 = 4{,}000$ kg m^{-3} was the density, $g_0 = 9.81$ m s^{-2} was the gravitational acceleration, $h_M = 2{,}867$ km was the thickness of the mantle, $\kappa_0 = 1 \times 10^{-6}$ m^2 s^{-1} was the thermal diffusivity, $\eta_0 = 1 \times 10^{21}$ Pa s was the viscosity. The subscript '0' indicated reference values. The coefficient of thermal expansion was depth-dependent, decreasing by a factor of about two over the thickness of the mantle (see refs 65,66). Based on these values, we obtained $Ra = 1.2 \times 10^8$ for M6. The Rayleigh number was varied across model cases (Extended Data Table 1).

Likewise, the dissipation number governed heat dissipation generated by shear heating. It was given by $Di = \frac{\alpha_0 g_0 R_0}{C_{p_0}}$, where $R_0 = 6{,}371$ km was Earth's radius and $C_{p_0} = 1{,}200$ J kg^{-1} K^{-1} was the reference heat capacity. The total rate of internal heating was estimated to be equal to 33.6 TW, accounting for contributions from both radioactive decay (~9–17 TW, ref. 67) and primordial heat dissipated through secular cooling of Earth's interior (~8–29 TW, ref. 67).

Depth-, composition-, temperature- and pressure-dependent radial viscosity was computed as

$$\eta = \eta(r)\, \eta_C \exp\left\{\frac{E_\eta + \rho_0 g Z_\eta (R_0 - r)}{R(T + T_{\text{off}})} - \frac{E_\eta + \rho_0 g Z_\eta (R_0 - R_C)}{R(T_{\text{CMB}} + T_{\text{off}})}\right\}, \quad (1)$$

The depth-dependent viscosity pre-factor $\eta(r)$ was equal to 2×10^{19} Pa s above 160 km depth and between 310–660 km depth (upper mantle), to 2×10^{18} Pa s in the asthenosphere between 60–310 km depth (6×10^{17} Pa s for model M6), 0.02, and 2×10^{20} Pa s in the lower mantle below 660 km depth (6×10^{20} Pa s for model M6; Extended Data Table 1). The compositional viscosity pre-factors η_C was equal to one for ambient mantle, to 100 for continental lithosphere (modelled as in ref. 62), and to 10 for the basal layer. r was the radius, $R_C = 3{,}504$ km was the radius of the core, $E_\eta = 284$ kJ mol^{-1} was the activation energy, $Z_\eta = 2.1 \times 10^{-6}$ m^3 mol^{-1} was the activation volume, $R = 8.31$ J mol^{-1} K^{-1} was the universal gas constant, T was the dimensional temperature, $T_{\text{off}} = 694$ K was a temperature offset and $T_{\text{CMB}} = 4{,}300$ K was the temperature at the core-mantle boundary. The viscosity structure, defined by the viscosity pre-factors, activation volume, activation energy and temperature offset produced viscosity

variations varying over three orders of magnitude across the model[32]. Although these contrasts were smaller than expected for the solid Earth[68], these lateral viscosity variations could be resolved at a spatial resolution at which time-dependent mantle flow can be computed using about 15,000 CPU hours per hundred million years on supercomputer Gadi.

We derived boundary conditions from the global tectonic reconstructions of ref. 58. We considered two reference frames for that tectonic reconstruction: the original paleomagnetic reference frame (PMAG, model M1) and a no-net-rotation reference frame (NNR), which was suitable to model mantle convection[32,69]. We analysed model results including dynamic topography, mantle temperature and composition fields in 20 million years increments.

We computed air-loaded dynamic topography at Earth's surface as $h = \frac{\sigma_{rr}}{\Delta\rho g}$ where g = 9.81 m s^{-2} was the acceleration of gravity and $\Delta\rho$ was the difference in densities between air (ρ_A = 0 kg m^{-3}) and the shallow upper mantle (ρ_{UM} = 3,320 kg m^{-3}). We considered free-slip boundary conditions, contributions from sources of buoyancy deeper than 350 km depth, and lateral viscosity variations deeper than 350 km depth.

Evaluating model success

As in refs 32,33,70, we first classified the present-day lower mantle structure as mapped by ten independent S-wave tomographic models[71-80] and predicted by six mantle flow models (M1-M6). To achieve this, we generated 196,965 evenly spaced points (~0.45°) on the surface and sampled mantle temperature (seismic velocity) every ~58 km between 1,000 and 2,800 km depths. We then used *k*-means[81] clustering to group these points into user-specified *k* clusters such that the within-cluster sum of squares (WCSS), i.e., the squared Euclidean distances between points and the centroid of the group, was minimised.

As in previous studies[32,33], we examined model success by computing three metrics (Extended Data Figure 1): (i) the predicted fractional area f_a of Earth's surface covered by clusters for hot BLOBS (for mantle flow models) and slow LLSVPs (for tomographic models), (ii) the global accuracy ($\overline{Acc}$) which was a measure of the spatial match between the present-

day mantle structure (clusters) predicted by mantle convection models and that averaged across ten independent tomographic models given by $\overline{Acc} = \frac{TP+TN}{A}$, where *TP* was the area of true positives representing spatial match between hot BLOBS and LLSVPs, *TN* the area of the true negatives measuring the spatial extent of cold basal mantle structure and high seismic velocity profiles and A was Earth's total surface area. For each model, the mean accuracy $\overline{Acc}$ represented the average across ten tomographic models, while for each tomographic model, $\overline{Acc}$ was computed as an average across the nine independent tomographic models; (iii) the time-averaged median angular distance $\tilde{\theta}$ between reconstructed volcanic eruption locations (LIPs and kimberlites as in ref. 32) from 320 Ma and the edge of hot BLOBS. The distance was taken as zero for eruption locations above a BLOBS or LLSVP. Smaller distances indicated a close spatial match between BLOBs or LLSVPs and volcanic eruptions, which was thought to be favourable[32,33,82]. Mantle flow models were deemed to perform better if all three metrics were within the range or close to the range for tomographic models (grey areas in Extended Data Figure 1).

Cluster analysis of dynamic topography

We generated a set of evenly spaced (~0.45º) points entirely covering present-day continents. We extracted dynamic topography at the reconstructed location of these points in 20 Myr intervals and rotated the results back into the present-day plate configuration. We used the continental blocks that continuously existed from 920 Ma to mask data for all other times so that the considered locations existed for all considered times. We used *k*-means clustering[81] as in ref. 83, to classify geographic regions that share a similar evolution of predicted dynamic topography.

We employed Silhouette[84] score, Davies-Bouldin Index[85] (DBI) and elbow[86] methods to decide on the appropriate number of clusters to consider (Extended Data Figure 2). The Silhouette score measured how similar a point was to its own cluster compared to other clusters. It combined intra-cluster cohesion and inter-cluster separation. Silhouette scores ranged from

minus one to one, with larger values indicating better-defined clusters. The DBI evaluated intra-cluster similarity and inter-cluster differences based on intra-cluster dispersion and inter-cluster distance. Lower scores indicated better clustering. It was computationally efficient but assumed compact, spherical clusters, making it less reliable for irregular shapes. The heuristic elbow method consisted of plotting the number of clusters (k) against the clustering cost (e.g., within-cluster sum of squares or WCCS) and identifying the 'elbow' point, at which the rate of improvement (decrease in WCCS) dropped off, suggesting the most appropriate k.

We identified the ideal number of clusters for all six model cases for both the Great Unconformity formation (920–420 Ma) and preservation (420–0 Ma) periods to be equal to either two or three (Extended Data Figure 2). We produced cluster maps for each model case and each cluster combinations (either two or three) and combined them in maps indicating model agreement with a score between zero and six out of six models. These 'vote' maps highlighted regions showing both formation and preservation of the Great Unconformity across model and cluster combinations (Extended Data Figure 6).

Mapping temporal evolution of preserved sediment flux and dynamic topography

We obtained the preserved sediment flux (sediment volume divided by time) from Neoproterozoic times (1.6 Ga) to the present for North America, South America, Africa, Eurasia and Australia from ref. 1. For the period 920–0 Ma, we scaled sediment flux by the present-day area of each considered continent as in ref. 1. We averaged continental dynamic topography for each continental block that continuously existed between 920–0 Ma (Extended Data Figure 9a) using the time periods at which sediment volume data were defined (Fig. 4a and Extended Data Figures 8-9).

To focus on long-term, long-wavelength processes, we filtered the preserved sediment data using time windows that corresponded to the periods of dynamic uplift and dynamic subsidence predicted for each continent. We then averaged the preserved sediment volume to

represent the sediment accumulation associated with each phase of dynamic topography (Fig 4b).

Methods references

1 Keller, C. B. *et al.* Neoproterozoic glacial origin of the Great Unconformity. *Proceedings of the National Academy of Sciences* **116**, 1136-1145 (2019). https://doi.org/10.1073/pnas.1804350116

31 Peters, S. E., Husson, J. M. & Czaplewski, J. Macrostrat: A Platform for Geological Data Integration and Deep-Time Earth Crust Research. *Geochemistry, Geophysics, Geosystems* **19**, 1393-1409 (2018). https://doi.org/https://doi.org/10.1029/2018GC007467

32 Flament, N., Bodur, Ö. F., Williams, S. E. & Merdith, A. S. Assembly of the basal mantle structure beneath Africa. *Nature* **603**, 846-851 (2022). https://doi.org/10.1038/s41586-022-04538-y

33 Cucchiaro, A., Flament, N., Arnould, M. & Cressie, N. Large volcanic eruptions are mostly sourced above mobile basal mantle structures. *Communications Earth & Environment* **6**, 538 (2025). https://doi.org/10.1038/s43247-025-02482-z

53 Zhong, S., McNamara, A., Tan, E., Moresi, L. & Gurnis, M. A benchmark study on mantle convection in a 3-D spherical shell using CitcomS. *Geochemistry, Geophysics, Geosystems* **9** (2008). https://doi.org/https://doi.org/10.1029/2008GC002048

54 Young, A. *et al.* Long-term Phanerozoic sea level change from solid Earth processes. *Earth and Planetary Science Letters* **584**, 117451 (2022). https://doi.org/https://doi.org/10.1016/j.epsl.2022.117451

55 Weber, J. & Flament, N. Factors Contributing to Slab Locations and Geometries in Reconstructions of Past Mantle Flow. *Geochemistry, Geophysics, Geosystems* **25**, e2023GC011313 (2024). https://doi.org/https://doi.org/10.1029/2023GC011313

56 Frasson, T., Labrosse, S., Nataf, H. C., Coltice, N. & Flament, N. On the impact of true polar wander on heat flux patterns at the core–mantle boundary. *Solid Earth* **15**, 617-637 (2024). https://doi.org/10.5194/se-15-617-2024

57 Bower, D. J., Gurnis, M. & Flament, N. Assimilating lithosphere and slab history in 4-D Earth models. *Physics of the Earth and Planetary Interiors* **238**, 8-22 (2015). https://doi.org/https://doi.org/10.1016/j.pepi.2014.10.013

58 Merdith, A. S. *et al.* Extending full-plate tectonic models into deep time: Linking the Neoproterozoic and the Phanerozoic. *Earth-Science Reviews* **214**, 103477 (2021). https://doi.org/https://doi.org/10.1016/j.earscirev.2020.103477

59 Gurnis, M. *et al.* Plate tectonic reconstructions with continuously closing plates. *Computers & Geosciences* **38**, 35-42 (2012). https://doi.org/https://doi.org/10.1016/j.cageo.2011.04.014

60 Chopelas, A. & Boehler, R. Thermal Expansivity in the Lower Mantle. *Geophysical Research Letters* **19**, 1983-1986 (1992). https://doi.org/Doi 10.1029/92gl02144

61 Williams, S., Wright, N. M., Cannon, J., Flament, N. & Müller, R. D. Reconstructing seafloor age distributions in lost ocean basins. *Geoscience Frontiers* **12**, 769-780 (2021). https://doi.org/https://doi.org/10.1016/j.gsf.2020.06.004

62 Flament, N. *et al.* Topographic asymmetry of the South Atlantic from global models of mantle flow and lithospheric stretching. *Earth and Planetary Science Letters* **387**, 107-119 (2014). https://doi.org/10.1016/j.epsl.2013.11.017

63 Bower, D. J., Gurnis, M. & Flament, N. Assimilating lithosphere and slab history in 4-D Earth models. *Physics of the Earth and Planetary Interiors* **238**, 8-22 (2015). https://doi.org/http://dx.doi.org/10.1016/j.pepi.2014.10.013

64 Dziewonski, A. M. & Anderson, D. L. Preliminary reference Earth model. *Physics of the Earth and Planetary Interiors* **25**, 297-356 (1981). https://doi.org/https://doi.org/10.1016/0031-9201(81)90046-7

65 Tosi, N., Yuen, D. A., de Koker, N. & Wentzcovitch, R. M. Mantle dynamics with pressure- and temperature-dependent thermal expansivity and conductivity. *Physics of*

the Earth and Planetary Interiors **217**, 48-58 (2013). https://doi.org/https://doi.org/10.1016/j.pepi.2013.02.004

66 Hassan, R., Flament, N., Gurnis, M., Bower, D. J. & Müller, D. Provenance of plumes in global convection models. *Geochemistry Geophysics Geosystems* **16**, 1465-1489 (2015). https://doi.org/10.1002/2015gc005751

67 Jaupart, C., Labrosse, S., Lucazeau, F. & Mareschal, J. C. in *Treatise on Geophysics* (ed Bercovici D.) 223-270 (Elsevier, 2015).

68 Stadler, G. *et al.* The dynamics of plate tectonics and mantle flow: from local to global scales. *Science* **329**, 1033-1038 (2010). https://doi.org/10.1126/science.1191223

69 Coltice, N., Gérault, M. & Ulvrová, M. A mantle convection perspective on global tectonics. *Earth-Science Reviews* **165**, 120-150 (2017). https://doi.org/https://doi.org/10.1016/j.earscirev.2016.11.006

70 Flament, N., Williams, S., Müller, R. D., Gurnis, M. & Bower, D. J. Origin and evolution of the deep thermochemical structure beneath Eurasia. *Nature Communications* **8**, 14164 (2017). https://doi.org/10.1038/ncomms14164

71 Mégnin, C. & Romanowicz, B. The three-dimensional shear velocity structure of the mantle from the inversion of body, surface and higher-mode waveforms. *Geophysical Journal International* **143**, 709-728 (2000). https://doi.org/10.1046/j.1365-246X.2000.00298.x

72 Houser, C., Masters, G., Shearer, P. & Laske, G. Shear and compressional velocity models of the mantle from cluster analysis of long-period waveforms. *Geophysical Journal International* **174**, 195-212 (2008). https://doi.org/10.1111/j.1365-246X.2008.03763.x

73 Kustowski, B., Ekström, G. & Dziewoński, A. M. Anisotropic shear-wave velocity structure of the Earth's mantle: A global model. *Journal of Geophysical Research: Solid Earth* **113**, B06306 (2008). https://doi.org/10.1029/2007jb005169

74 Ritsema, J., Deuss, A., van Heijst, H. J. & Woodhouse, J. H. S40RTS: a degree-40 shear-velocity model for the mantle from new Rayleigh wave dispersion, teleseismic traveltime and normal-mode splitting function measurements. *Geophysical Journal International* **184**, 1223-1236 (2011). https://doi.org/10.1111/j.1365-246X.2010.04884.x

75 Auer, L., Boschi, L., Becker, T. W., Nissen-Meyer, T. & Giardini, D. Savani: A variable resolution whole-mantle model of anisotropic shear velocity variations based on multiple data sets. *Journal of Geophysical Research: Solid Earth* **119**, 3006-3034 (2014). https://doi.org/10.1002/2013jb010773

76 French, S. W. & Romanowicz, B. A. Whole-mantle radially anisotropic shear velocity structure from spectral-element waveform tomography. *Geophysical Journal International* **199**, 1303-1327 (2014). https://doi.org/10.1093/gji/ggu334

77 Thrastarson, S., van Herwaarden, D. P., Noe, S., Josef Schiller, C. & Fichtner, A. REVEAL: A Global Full-Waveform Inversion Model. *Bulletin of the Seismological Society of America* **114**, 1392-1406 (2024). https://doi.org/10.1785/0120230273

78 Cui, C. *et al.* GLAD-M35: a joint P and S global tomographic model with uncertainty quantification. *Geophysical Journal International* **239**, 478-502 (2024). https://doi.org/10.1093/gji/ggae270

79 Montelli, R., Nolet, G., Dahlen, F. A. & Masters, G. A catalogue of deep mantle plumes: New results from finite-frequency tomography. *Geochemistry, Geophysics, Geosystems* **7** (2006). https://doi.org/https://doi.org/10.1029/2006GC001248

80 Simmons, N. A., Forte, A. M., Boschi, L. & Grand, S. P. GyPSuM: A joint tomographic model of mantle density and seismic wave speeds. *Journal of Geophysical Research: Solid Earth* **115** (2010). https://doi.org/https://doi.org/10.1029/2010JB007631

81 MacQueen, J. Vol. 1 281-297 (University of California Press, 1967).

82 Torsvik, T. H., Burke, K., Steinberger, B., Webb, S. J. & Ashwal, L. D. Diamonds sampled by plumes from the core–mantle boundary. *Nature* **466**, 352-355 (2010). https://doi.org/10.1038/nature09216

83 Müller, R. D., Hassan, R., Gurnis, M., Flament, N. & Williams, S. E. Dynamic topography of passive continental margins and their hinterlands since the Cretaceous. *Gondwana Research* **53**, 225-251 (2018). https://doi.org/https://doi.org/10.1016/j.gr.2017.04.028

84 Rousseeuw, P. J. Silhouettes: A graphical aid to the interpretation and validation of cluster analysis. *Journal of Computational and Applied Mathematics* **20**, 53-65 (1987). https://doi.org/https://doi.org/10.1016/0377-0427(87)90125-7

85 Davies, D. L. & Bouldin, D. W. A Cluster Separation Measure. *IEEE Transactions on Pattern Analysis and Machine Intelligence* **PAMI-1**, 224-227 (1979). https://doi.org/10.1109/TPAMI.1979.4766909

86 Thorndike, R. L. Who Belongs in the Family? *Psychometrika* **18**, 267-276 (1953). https://doi.org/10.1007/BF02289263

Acknowledgements

SD and NF were supported by Australian Research Council grant FT230100001. This research was undertaken with the assistance of resources from the National Computational Infrastructure (NCI), which is supported by the Australian Government. Access to NCI was partly supported by resources and services from the University of Wollongong (UOW). We thank C. V. Murray-Wallace and T. Cohen for comments on the manuscript.

Author contributions (CRediT author statement)

Santosh Dhungana: Conceptualization, Methodology, Software, Validation, Formal Analysis, Investigation, Writing – Original Draft, Visualization. **Nicolas Flament:** Conceptualization, Methodology, Validation, Formal Analysis, Investigation, Resources, Writing – Original Draft, Visualization, Supervision, Funding Acquisition.

Competing interests

The authors declare no competing interests.

Correspondence and requests for materials should be addressed to N. F.

Supplementary information is available for this paper.

Data availability

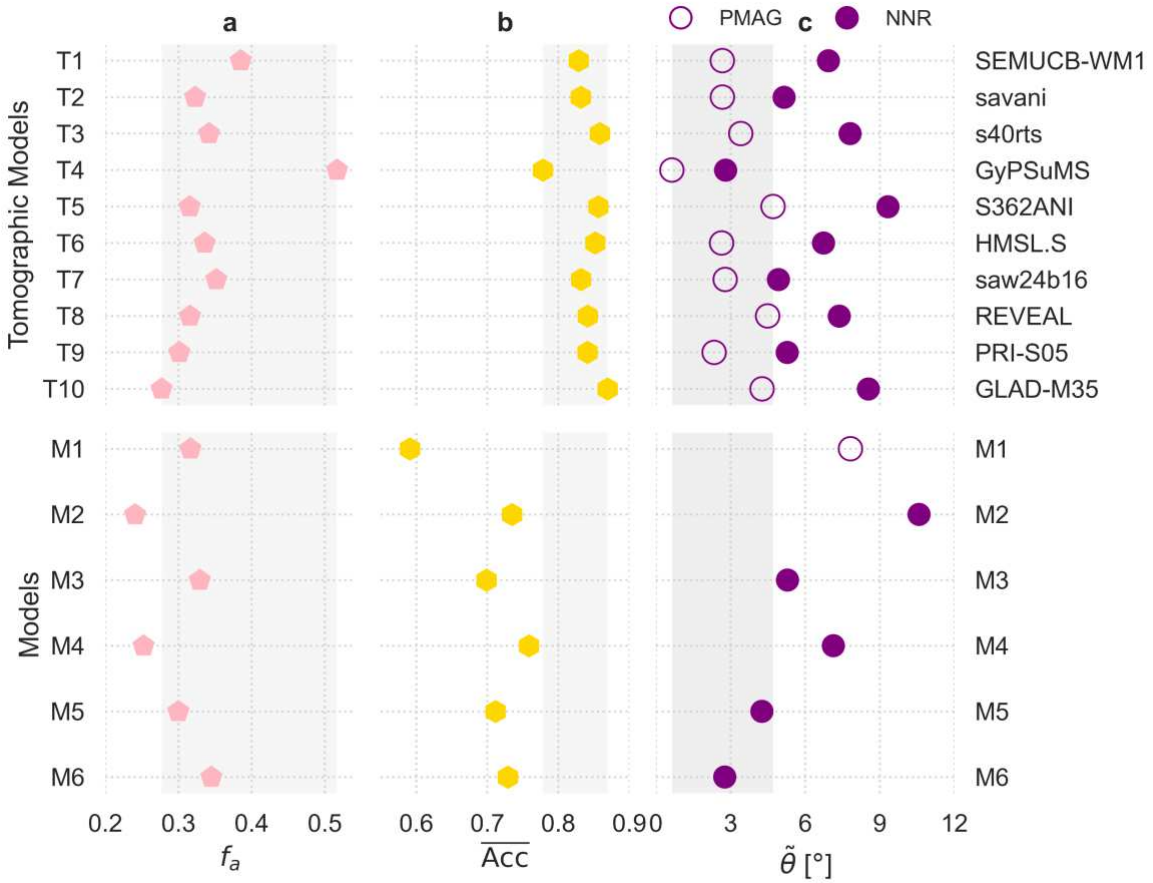
Data generated for this study can be accessed at: https://doi.org/10.5281/zenodo.17773494.

Code availability

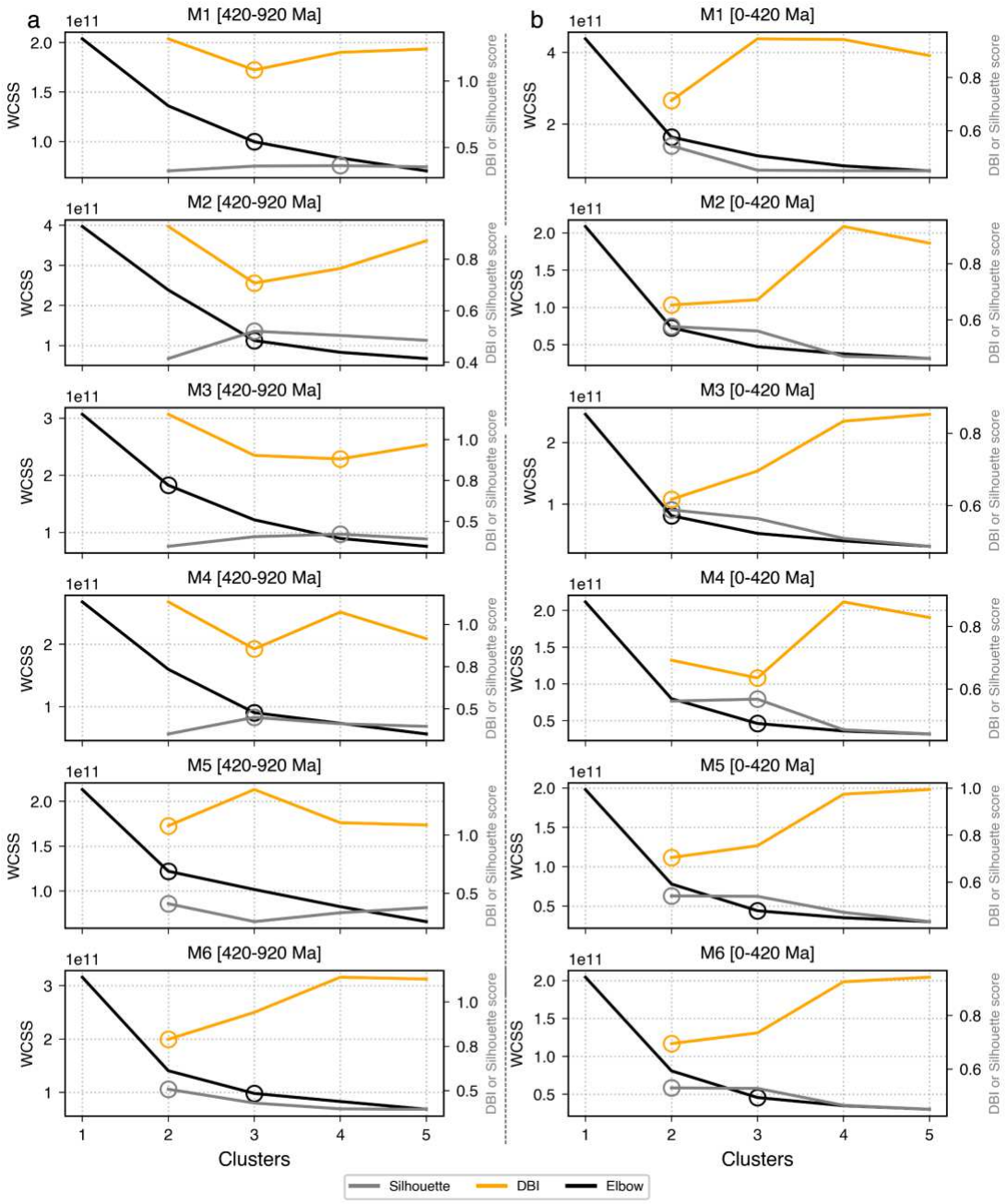
The code used to run mantle models is available at https://github.com/EarthByte/citcoms. The Jupyter notebooks and Python scripts written to process data and generate Figures 1–4 and Extended Data Figures 1–9 are available at: https://doi.org/10.5281/zenodo.17773494. Figures 1–3 and Extended Data Figures 3–7 were created using the open-source Python library PyGMT (v.0.13.0), a Pythonic interface for the Generic Mapping Tools (GMT)[87] and Figure 4 and Extended Data Figures 1–2, 8–9 were created using the open-source Python library Matplotlib[88] (v.3.8.3).

Extended Data Table 1 | Input Parameters and boundary conditions for mantle flow model cases.

Model name	Reconstruction	Warm up (Myr)	Rayleigh number	$\eta_{\mathrm{asth}}(r)$ (Pa s)	$\eta_{\mathrm{LM}}(r)$ (Pa s)	$\delta\rho_b$
M1	NR	0	7.84×10^7	2×10^{18}	2×10^{20}	1.0%
M2	NNR	200	7.84×10^7	2×10^{18}	2×10^{20}	1.0%
M3	NNR	0	7.84×10^7	2×10^{18}	2×10^{20}	0.5%
M5	NNR	250	1.00×10^8	2×10^{18}	2×10^{20}	1.7%
M4	NNR	0	7.84×10^7	2×10^{18}	2×10^{20}	1.0%
M6	NNR	250	1.20×10^8	6×10^{17}	6×10^{20}	2.4%



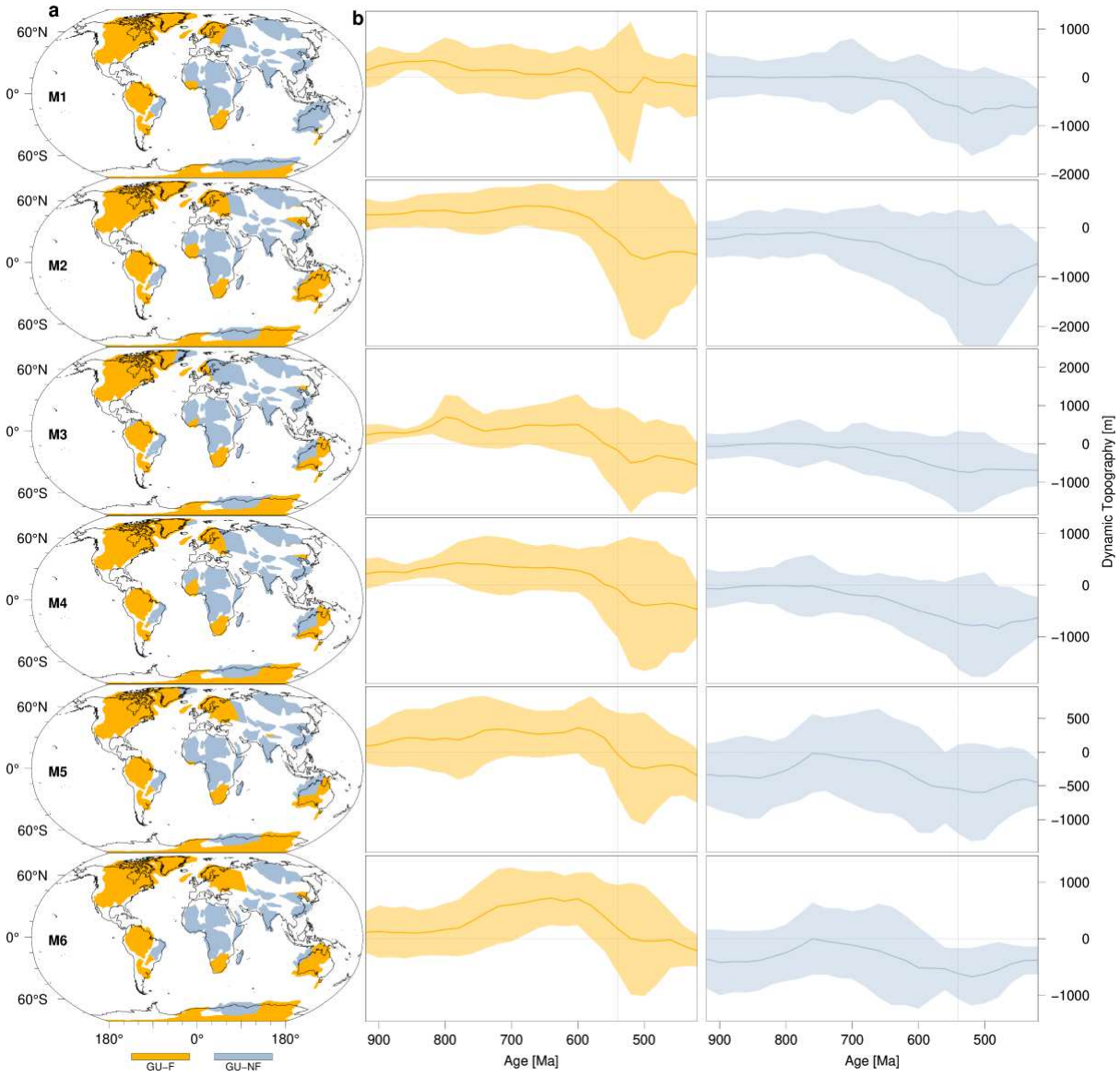
Extended Data Figure 1 | Spatial match between BLOBS predicted by mantle flow models and LLSVPs inferred from S-wave tomographic models[71-80] **and BLOBS and LLSVP proximity to volcanic eruptions. a**, Fractional area f_a of deep mantle cluster maps covered by BLOBS (in flow models, present day) and LLSVPs (in tomographic models). **b**, Spatial match ($\overline{Acc}$) between LLSVPs of a given tomographic model and the averaged LLSVPs from other nine tomographic models, and present-day BLOBS for a given model case and LLSVPs averaged across ten tomographic models. **c**, Time-averaged median of minimum angular distances $\tilde{\theta}$ between BLOBs and volcanic eruptions from 320 Ma. In **a-c**, the first row shows results for ten tomographic models (stationary LLSVPs), and the last row shows results for six flow models (mobile BLOBs) across which parameters are varied as indicated. 'T1-T10': tomographic models 1-10; 'M1-M6': mantle flow model Cases 1-6. The grey shadings in **a-c** highlight the range of results for tomographic models.



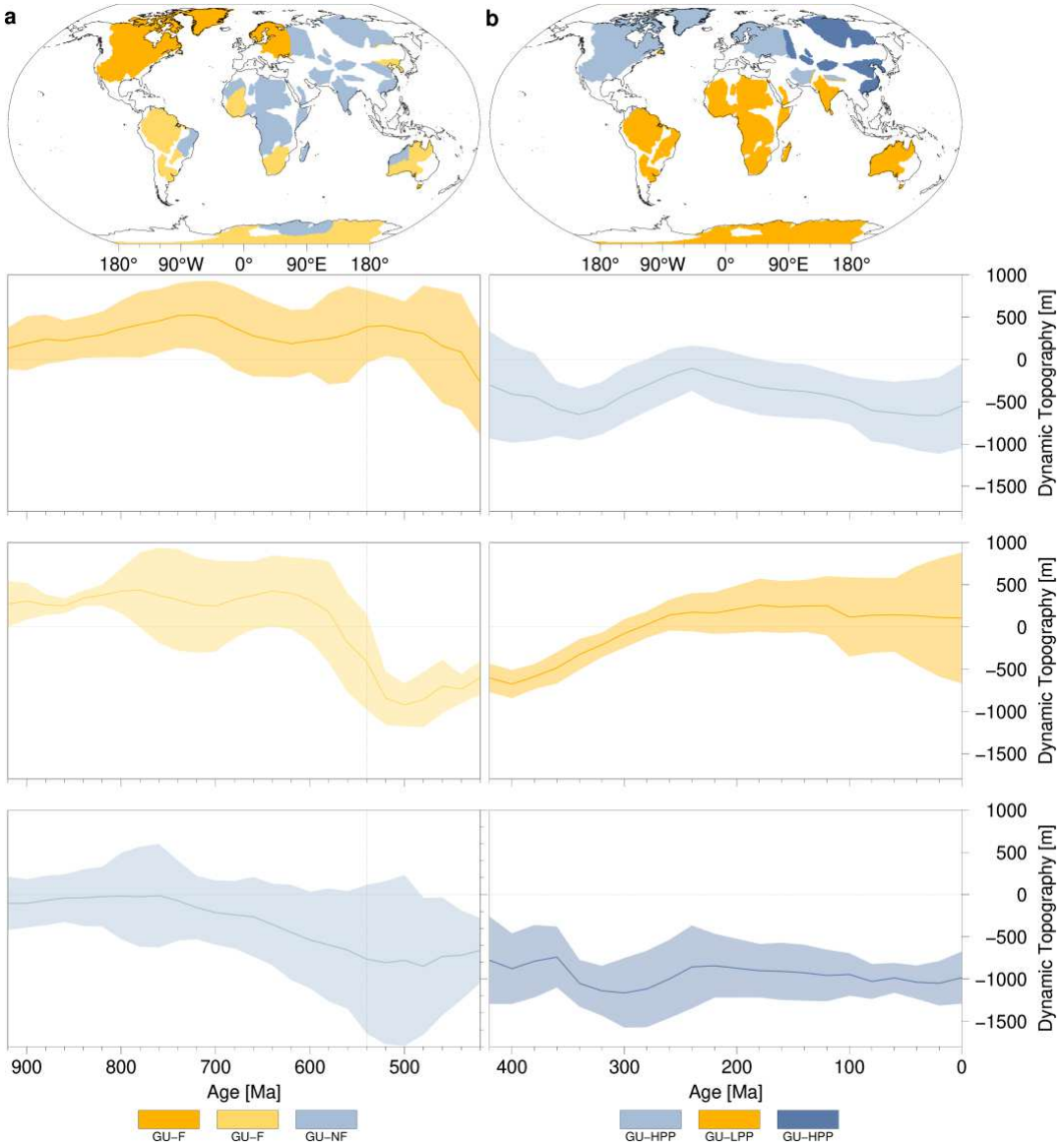
775

776 **Extended Data Figure 2 | Statistical determination of the number of clusters based on the**
777 **Silhouette score, Davies-Bouldin Index (DBI) and elbow methods. a-b,** Scores for each
778 metric against the number of clusters for the data set corresponding to 920–420 Ma (**a**) and
779 420–0 Ma (**b**). Coloured rounded markers in **a-b** indicate the optimal number of clusters based
780 on the score of each metric (grey: Silhouette score, orange: DBI and blue: elbow method).
781 Maximum score, minimum score and bends in plot are the criteria used by Silhouette, DBI and
782 elbow method respectively to determine optimal number of clusters. M1-M6 denote the six
783 considered model cases. Cartesian projection in (**a-b**).

784



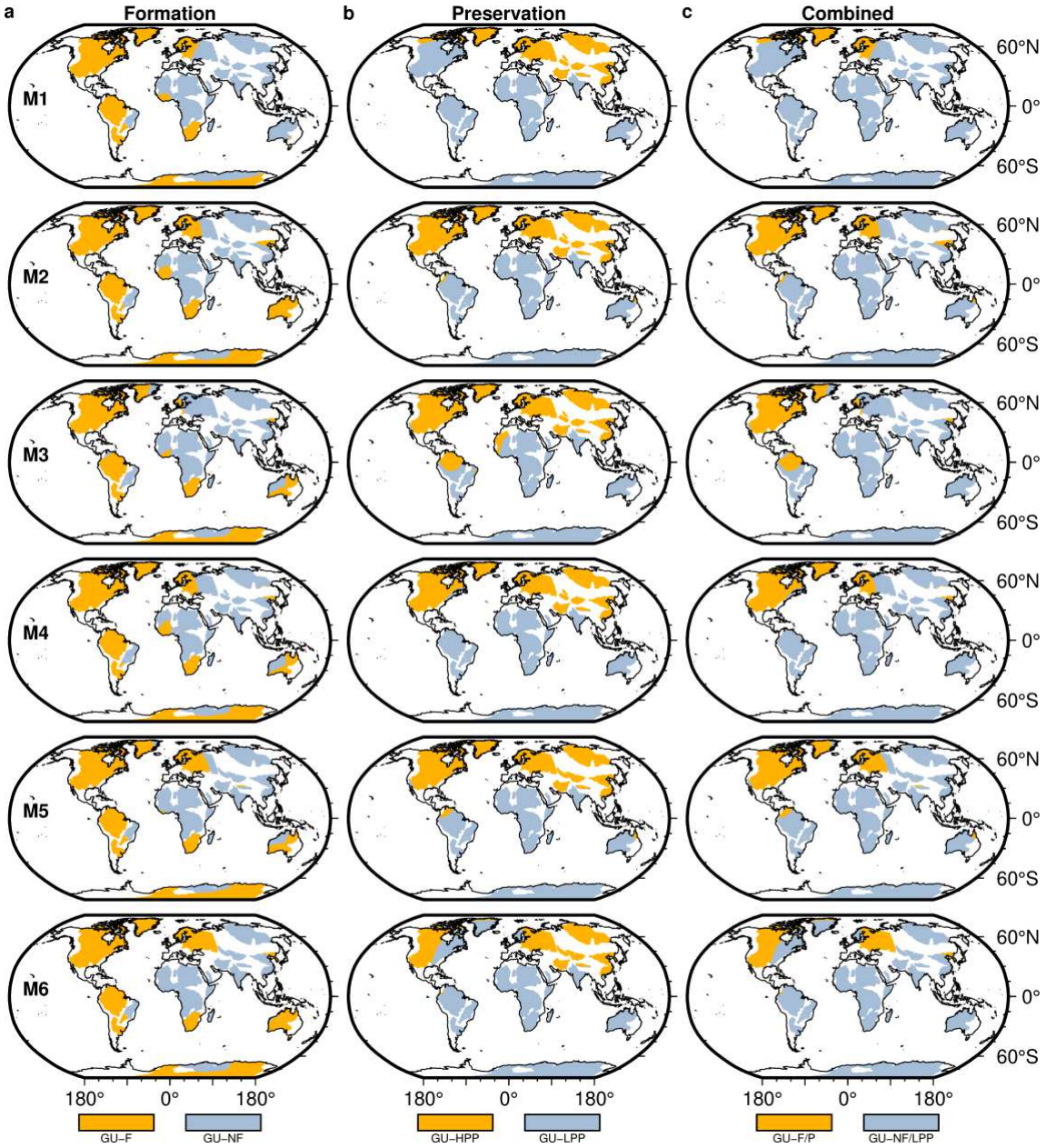
Extended Data Figure 3 | Cluster analysis of dynamic topography between 920–420 Ma for all models. a, Spatial distribution of two clusters GU-F ('Great Unconformity - Formation') and GU-NF ('Great Unconformity - No Formation') revealed by *k-means* cluster analysis showing continental blocks that existed from 920 Ma in their present-day location. Robinson projection at Earth's surface. **b**, Temporal evolution of averaged continental dynamic topography for each cluster in (**a**) with ± 2 standard deviation envelopes. The vertical dashed grey line in (**b**) is the start of Cambrian times, and the horizontal dashed line the datum for the dynamic topography.



795

796 **Extended Data Figure 4 | Cluster analysis of dynamic topography for model M4 between**
797 **920–420 Ma and 420–0 Ma. a-b,** Spatial distribution of three clusters revealed by *k*-means
798 cluster analysis (top row) and their temporal evolution with ± 2 standard deviation envelopes
799 for 920–420 Ma (**a**) and 420–0 Ma (**b**) for continental blocks that existed from 920 Ma in their
800 present-day location. The clusters are classified as two GU-F ('Great Unconformity -
801 Formation') clusters and one GU-NF ('Great Unconformity - No Formation') clusters for 920–
802 420 Ma (**a**) and two GU-HPP ('Great Unconformity - High Preservation Potential') clusters
803 and one GU-LPP ('Great Unconformity - Low Preservation Potential') cluster for 420–0 Ma
804 (**b**). The vertical dashed grey line in (**a-b**) is the start of Cambrian times, and the horizontal
805 dashed line the datum for the dynamic topography. Robinson projection at Earth's surface for
806 the two top panels.

807



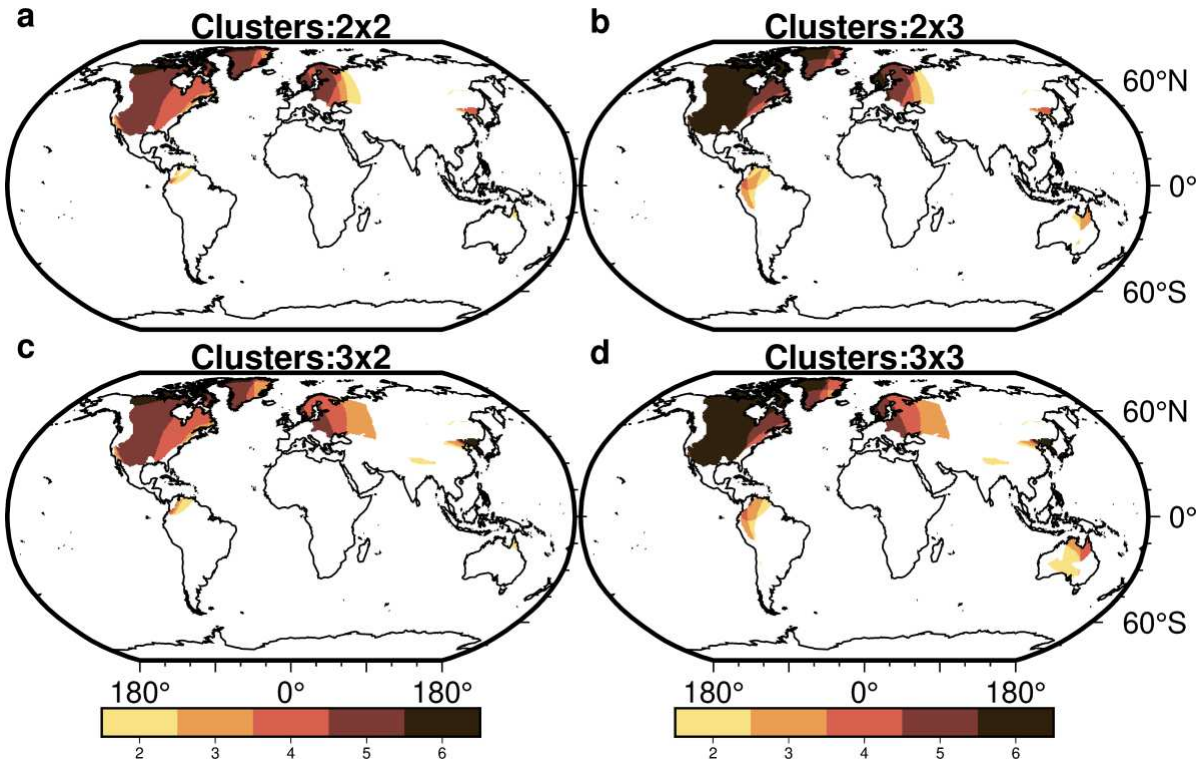
808

809 **Extended Data Figure 5 | Spatial distribution of dynamic topography clusters for all**
810 **models during the Great Unconformity formation (920–420 Ma) and preservation (420–**
811 **0 Ma) periods. a-c,** Spatial distribution of two clusters revealed by *k*-means clustering for
812 continental blocks that existed from 920 Ma in their present-day configuration with GU-F and
813 GU-NF for period of 920–420 Ma (**a**), GU-HPP and GU-LPP between 420–0 Ma (**b**) and
814 regions forming and preserving the Great Unconformity (GU-F/P) and regions with low
815 preservation potential (GU-NF/LPP) (**c**) obtained by combining (**a**) and (**b**). Robinson
816 projection at Earth's surface.

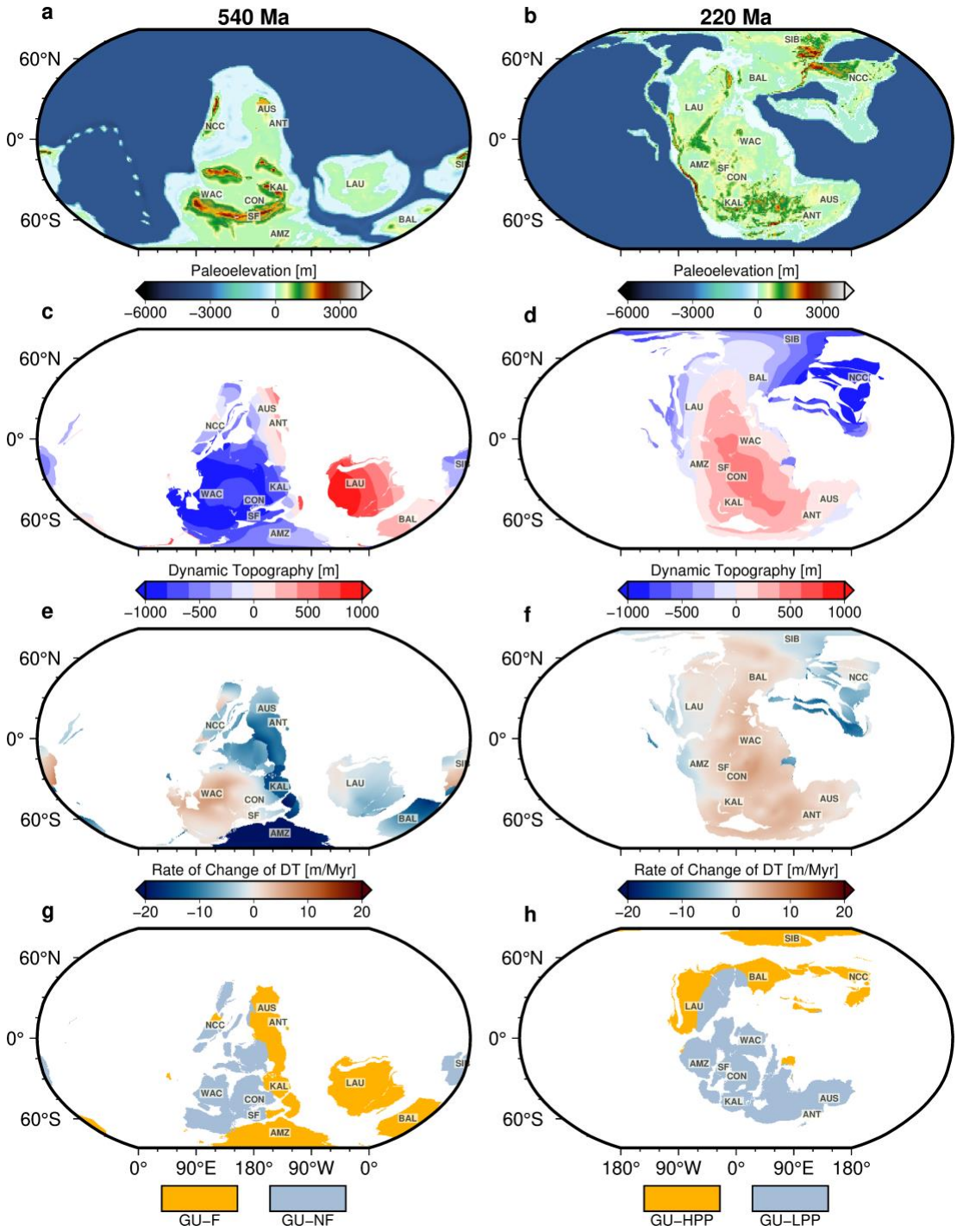
817

818

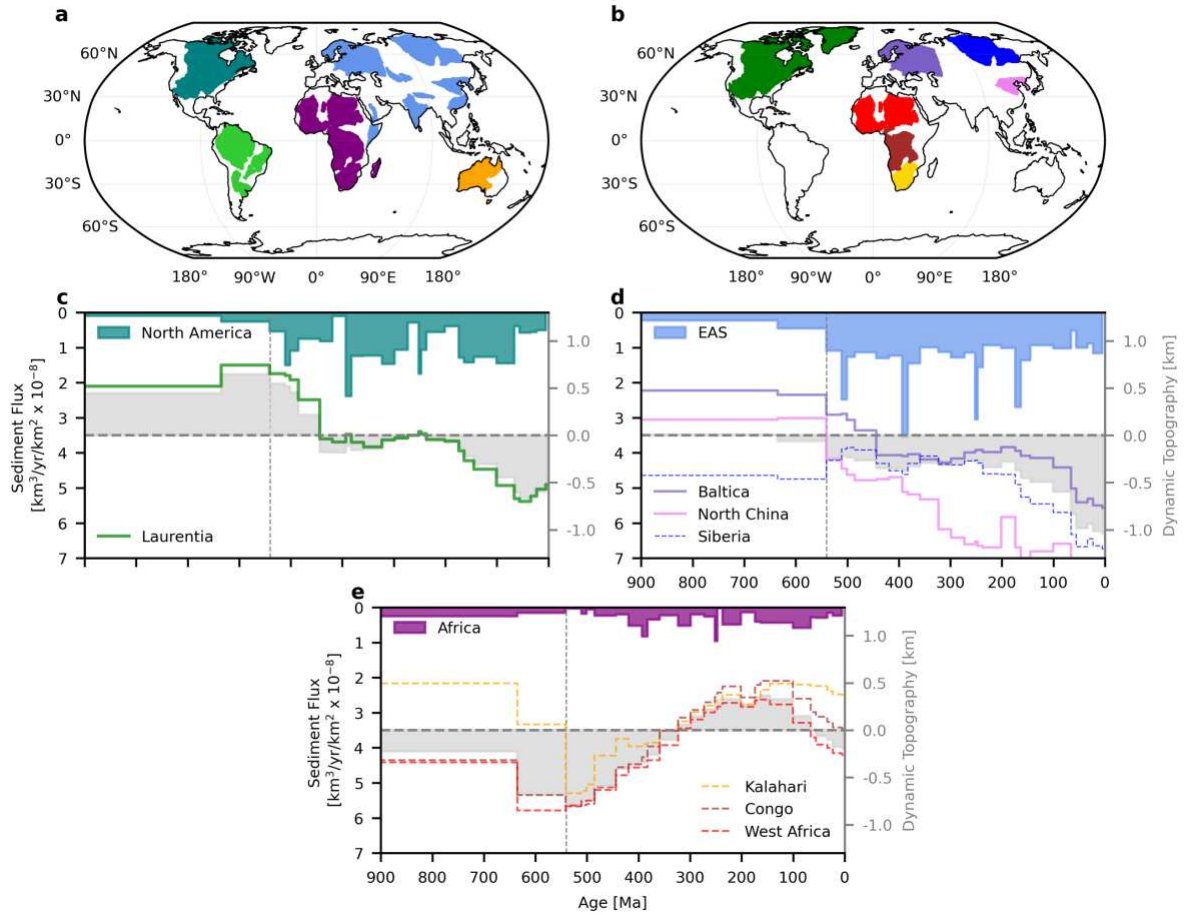
819



Extended Data Figure 6 | Vote maps showing spatial regions forming and preserving the Great Unconformity across all model and cluster combinations. a-d, Maps showing the areas in which the Great Unconformity is predicted to have formed between 920–420 Ma and been preserved between 420–0 Ma using **a**, two clusters for each period; **b**, two clusters for 920–420 Ma and three clusters for 420–0 Ma; **c**, three clusters for 920–420 Ma and two clusters for 420–0 Ma; and **d**, three clusters for 920–420 Ma and three clusters for 420–0 Ma. Colours indicate model agreement ('vote map'), with a score equal to six indicating consensus across all models for a region. Robinson projection at Earth's surface.



Extended Data Figure 7 | Paleo-elevations, dynamic topography, dynamic topography rate of change and reconstructed clusters in a paleomagnetic frame of reference[89]. a-b, Paleo-elevation maps from ref. 89 at 540 Ma (**a**) and 220 Ma (**b**). **c-f**, Predicted dynamic topography and long-term dynamic topography rate of change reconstructed at 540 Ma (**c**, **e**) and 220 Ma (**d**, **f**). **g-h**, Dynamic topography clusters (**g**) at 540 Ma and at 220 Ma (**h**). In **a-h** abbreviated labels indicate 'AMZ': Amazonia, 'ANT': Antarctica, 'AUS': Australia, 'BAL': Baltica, 'CON': Congo, KAL: Kalahari, LAU: Laurentia, 'NCC': North China, 'SF': São Francisco, 'SIB': Siberia and 'WAC': West Africa. Robinson projection at Earth's surface.



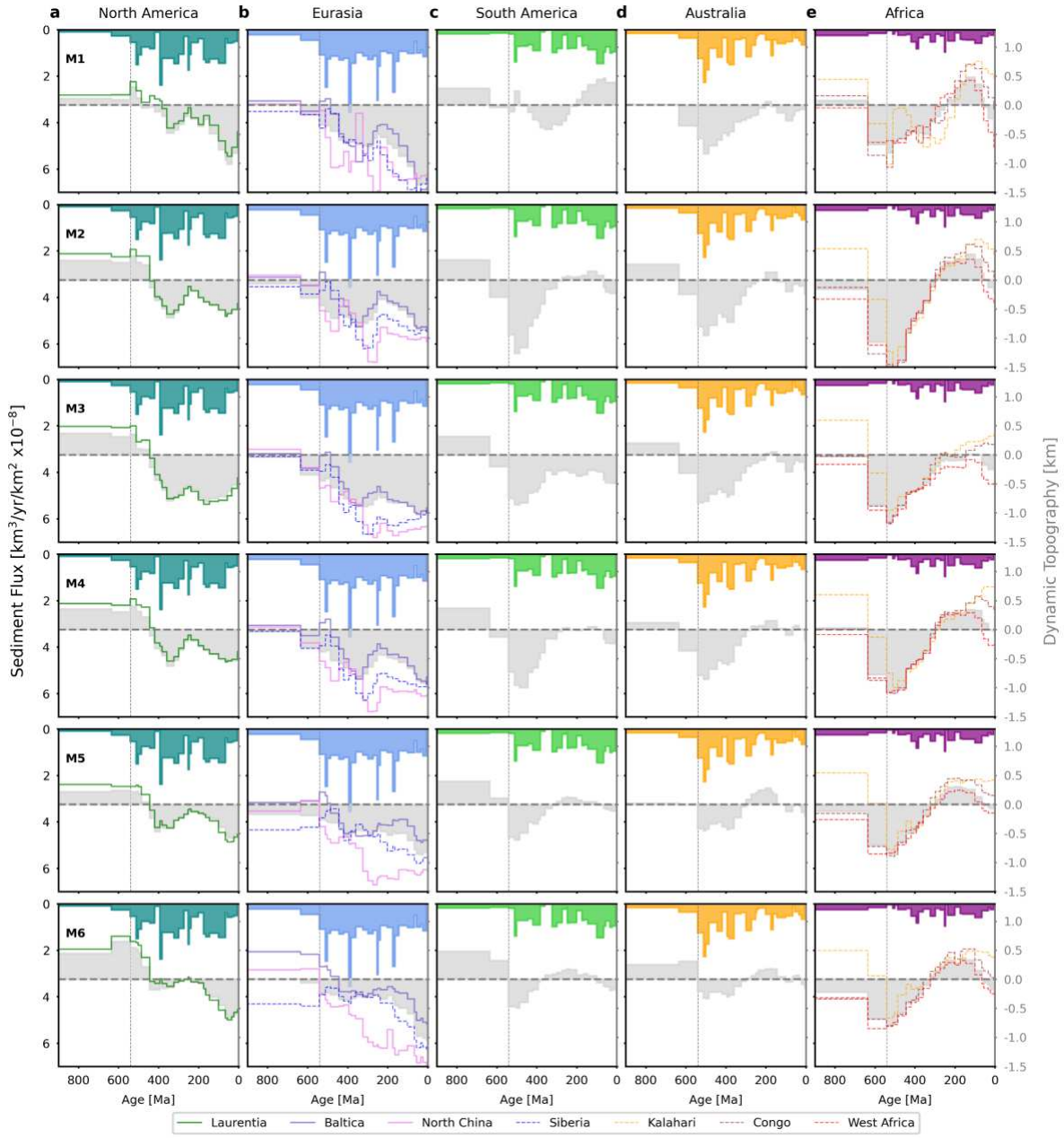
839

840 **Extended Data Figure 8 | Preserved sediments flux and dynamic topography across**
841 **continents and continental blocks. a**, Continents considered to determine preserved sediment
842 flux[1,13]. **b**, Selected continental blocks continuously existing from 920 Ma. **c-e**, Temporal
843 evolution of the sediment volume per year and per unit continental area (increasing down), and
844 average dynamic topography across North America (**c**), Eurasia (**d**) and Africa (**e**). The
845 coloured solid and dotted lines represent the temporal evolution of dynamic topography for the
846 continental blocks shown in (**b**).

847

848

849



Extended Data Figure 9 | Temporal evolution of volumetric flux of preserved sediments compiled by ref. 13 (obtained from ref. 1) and average dynamic topography cycles across continents between 920–0 Ma for all mantle flow models. a-e, Temporal evolution of preserved volume of sediment per year and per unit continental area (increasing down), and dynamic topography for each model averaged at time steps corresponding to the sediment preservation data[1,13] across Laurentia (**a**), Amazonia (**b**), Australia (**c**), Eurasia (**d**) and Africa (**e**). Coloured solid and dotted lines indicate the temporal evolution of dynamic topography for selected continental blocks in Eurasia and Africa.

Supplementary material

Supplementary Video 1 | Predicted joint evolution of dynamic topography and mantle temperature from 920 Ma. a, Dynamic topography. **b**, Mantle temperature anomaly at 2,677 km depth. In **a**-**b**, cyan lines represent mid-ocean ridges and transform faults, and magenta lines represent subduction zones with triangles on the overriding plate. The green lines with diamonds are great circles transects A-A' shown in **e**-**f**. The length of the great circle depends on its latitudinal position. Robinson projection at Earth's surface. Transparent grey polygons represent continental blocks, with labels 'AMZ': Amazonia, 'ANT': Antarctica, 'AUS': Australia, 'BAL': Baltica, 'CON': Congo, KAL: Kalahari, 'LAU': Laurentia, 'NCC': North China, 'SF': São Francisco, 'SIB': Siberia and 'WAC': West Africa. **c**, Cross-section of temperature anomalies and dynamic topography across Laurentia (transect A-A'). The dynamic topography line (not to scale) above the cross-section plot illustrates spatial variations, with positive values shown in red and negative values in blue. The maximum and minimum values of dynamic topography along the transect are reported at their respective locations above the line. The black solid line indicates 2,667 km depth. Polar projection of longitude and depth. The colour bar in (**c**) is the temperature anomaly scale for **b**-**c.**

Extended Data Figures references

1 Keller, C. B. *et al.* Neoproterozoic glacial origin of the Great Unconformity. *Proceedings of the National Academy of Sciences* **116**, 1136-1145 (2019). https://doi.org/10.1073/pnas.1804350116

13 Ronov, A. B., Khain, V. E., Balukhovsky, A. N. & Seslavinsky, K. B. Quantitative analysis of Phanerozoic sedimentation. *Sedimentary Geology* **25**, 311-325 (1980). https://doi.org/https://doi.org/10.1016/0037-0738(80)90067-6

71 Mégnin, C. & Romanowicz, B. The three-dimensional shear velocity structure of the mantle from the inversion of body, surface and higher-mode waveforms. *Geophysical Journal International* **143**, 709-728 (2000). https://doi.org/10.1046/j.1365-246X.2000.00298.x

72 Houser, C., Masters, G., Shearer, P. & Laske, G. Shear and compressional velocity models of the mantle from cluster analysis of long-period waveforms. *Geophysical Journal International* **174**, 195-212 (2008). https://doi.org/10.1111/j.1365-246X.2008.03763.x

73 Kustowski, B., Ekström, G. & Dziewoński, A. M. Anisotropic shear-wave velocity structure of the Earth's mantle: A global model. *Journal of Geophysical Research: Solid Earth* **113**, B06306 (2008). https://doi.org/10.1029/2007jb005169

74 Ritsema, J., Deuss, A., van Heijst, H. J. & Woodhouse, J. H. S40RTS: a degree-40 shear-velocity model for the mantle from new Rayleigh wave dispersion, teleseismic traveltime and normal-mode splitting function measurements. *Geophysical Journal International* **184**, 1223-1236 (2011). https://doi.org/10.1111/j.1365-246X.2010.04884.x

75 Auer, L., Boschi, L., Becker, T. W., Nissen-Meyer, T. & Giardini, D. Savani: A variable resolution whole-mantle model of anisotropic shear velocity variations based on multiple data sets. *Journal of Geophysical Research: Solid Earth* **119**, 3006-3034 (2014). https://doi.org/10.1002/2013jb010773

76 French, S. W. & Romanowicz, B. A. Whole-mantle radially anisotropic shear velocity structure from spectral-element waveform tomography. *Geophysical Journal International* **199**, 1303-1327 (2014). https://doi.org/10.1093/gji/ggu334

77 Thrastarson, S., van Herwaarden, D. P., Noe, S., Josef Schiller, C. & Fichtner, A. REVEAL: A Global Full-Waveform Inversion Model. *Bulletin of the Seismological Society of America* **114**, 1392-1406 (2024). https://doi.org/10.1785/0120230273

78 Cui, C. *et al.* GLAD-M35: a joint P and S global tomographic model with uncertainty quantification. *Geophysical Journal International* **239**, 478-502 (2024). https://doi.org/10.1093/gji/ggae270

79 Montelli, R., Nolet, G., Dahlen, F. A. & Masters, G. A catalogue of deep mantle plumes: New results from finite-frequency tomography. *Geochemistry, Geophysics, Geosystems* **7** (2006). https://doi.org/https://doi.org/10.1029/2006GC001248

80 Simmons, N. A., Forte, A. M., Boschi, L. & Grand, S. P. GyPSuM: A joint tomographic model of mantle density and seismic wave speeds. *Journal of Geophysical Research: Solid Earth* **115** (2010). https://doi.org/https://doi.org/10.1029/2010JB007631

87 Wessel, P. *et al.* The Generic Mapping Tools Version 6. *Geochemistry, Geophysics, Geosystems* **20**, 5556-5564 (2019). https://doi.org/https://doi.org/10.1029/2019GC008515

88 Hunter, J. D. Matplotlib: A 2D Graphics Environment. *Computing in Science & Engineering* **9**, 90-95 (2007). https://doi.org/10.1109/MCSE.2007.55

89 Scotese, C. R. & Wright, N. M. PALEOMAP Paleodigital Elevation Models (PaleoDEMS) for the Phanerozoic. (2018). https://doi.org/10.5281/zenodo.5460860

Supplementary Files

This is a list of supplementary files associated with this preprint. Click to download.

- SupplementaryVideo1LAU.mp4